(Note: this was previously the pre-print version, but it is now the final, published version of the paper.)

Research Article

Coupled Calorimetry and Resistivity Measurements, in Conjunction with an Emended and More Complete Phase Diagram of the Palladium–Isotopic Hydrogen System

M.R. Staker*

Department of Engineering, Loyola University Maryland, 4501 North Charles St, Baltimore, MD 21210, USA

Abstract

Results of a calorimetric study established the energy produced, over and above input energy, from electrolytic loading of deuterium into Pd was 150 MJ/cm^3 of Pd (14 000 eV/Pd atom) for a 46 day period. High fugacity of deuterium was developed in unalloyed palladium via electrolysis (0.5 mol electrolyte of lithium deuteroxide, LiOD) with the use of an independent electromigration current. In situ resistivity measurements of Pd were used to assay activity of D in the Pd lattice (ratio of D/Pd) and employed as an indicator of phase changes. During this period, two run-away events were triggered by suddenly increasing current density resulting in 100% excess power (2.4 W output with 1.2 W input) and necessitating temporary cut back in electrolysis current. The average excess power (excluding run-away) ranged from 4.7 ± 0.15 to 9.6 ± 0.30% of input power while input power ranged from 2.000 to 3.450 W, confirming the Fleischmann–Pons effect. The precision was: Power In = ± 0.0005 W; $\Delta T = \pm 0.05°$C; Power Out = ±0.015 W for an overall precision of ±0.5%. High fugacity was required for these results, and the triggered run-away events required even higher fugacity. Using thermodynamic energy balance, it was found that the energy release was of such magnitude that the source of the energy is from a nuclear source; however, the exact reaction was not determined in this work. X-ray diffraction results from the recent literature, rules for phase diagram construction, and thermodynamic stability requirements necessitate revisions of the phase diagram, with addition of three *thermodynamically stable* phases of the superabundant vacancy (SAV) type. These phases, each requiring high fugacity, are: γ (Pd$_7$ VacD$_{6-8}$), δ (Pd$_3$VacD$_4$- octahedral), δ' (Pd$_3$ VacD$_4$-tetrahedral). The emended palladium–isotopic hydrogen phase diagram is presented. The excess heat condition supports portions of the cathode being in the ordered δ-phase (Pd$_3$VacD$_4$- octahedral), while a drop in resistance of the Pd cathode during increasing temperature and excess heat production strongly indicates portions of the cathode also transformed . . . (continued in the next page)
© 2019 ISCMNS. All rights reserved. ISSN 2227-3123

Keywords: Calorimetry, Electrolysis, Nuclear energy, Palladium–isotopic hydrogen phase diagram, Resistivity, Superabundant vacancy structures

*E-mail: m.r.staker@alum.mit.edu (best) or mstaker@loyola.edu; Tel.: 410 617 5188.

(continued from title page)... to the ordered δ'-phase (Pd_3VacD_4 - tetrahedral). A dislocation mechanism is presented for creation of vacancies and mobilizing them by electromigration because of their attraction to D^+ ions which aids the formation of SAV-phases. Extending SAV unit cells to the periodic lattice epiphanates δ as the nuclear active state. The lattice of the decreased resistance phase, δ', reveals extensive pathways of low resistance and a potential connection to the superconductivity phase of PdH/PdD.

1. Introduction

Modifications of properties in metals and alloys, apart from hydrogen embrittlement and degradation (reviewed by Robertson et al. [1]), by introducing hydrogen to high activity include: increased and decreased resistivity [2], induced ferromagnetism [3], optical property changes [4,5], increased lattice atom mobility [6,7], induced ordering [8,9], increased levels of vacancies [10,11], and even vacancies at concentrations near 25% [12–22], called superabundant vacancies (SAV). SAV formation in face centered cubic (FCC) metals changes the unit cells from FCC to simple cubic (SC) with vacancies (Vac) at all corner atoms of the FCC unit cell. This Vac ordering is similar to the gold (Au) ordering in copper–gold (Cu_3Au). In palladium (Pd), ordered SAV structures are: $Pd_3Vac_1D_x$ (δ or δ'-phases) [15,21] where x is between 4 and 8, and $Pd_7Vac_1D_{6-8}$ (γ-phase) [22]. Isotopic hydrogen atoms (protium (H), deuterium (D), or tritium (T)) occupy the octahedral interstitial sites (δ-phase) singly or as a pair of closely spaced atoms in $Pd_3Vac_1D_x$ [15,21] and/or occupy tetrahedral sites (δ'-phase) [23,24]. (Naming here follows the convention of phase diagram construction of phases left to right in order of the Greek alphabet.) SAV are observed in other metals/alloys beside Pd and nickel Ni and include: Fe, Mn, Ti, Zr, Nb, Al, Cu, Mo, Cr, Co, Ag, Au, Rh, Pt, Ir, Pu, Pd–Rh alloys, Pd–Ag alloys, and Cu–Ni alloys. SAV have been produced by the following methods: wet electrolysis, high-temperature with high-pressure gas via anvil compression, co-deposited electrolysis, solid state electrolysis (dry electrolyte), ion beam implantation, and plasma-injection. Eliaz et al. [25] have reviewed hydrogen-assisted processing of materials. Links between processing, structure and properties is continuously sought by metallurgists and material scientists. Does increased space between atoms along unit cell edges change conductivity, electron mobility, and redistribution of electron density (Schrodinger equation), and thereby enable nuclear reactions inside a lattice along these edges? The first purpose of this investigation is to position the new phases appropriately on the Pd–isotopic hydrogen equilibrium phase diagram. The second purpose is to investigate if electrolytically loading of D into Pd produces excess heat (more heat out than in) consistently, benefiting from electromigration and high dislocation density from plastic deformation with an associated increase in vacancies. A related purpose is to explore if SAV favor nuclear reactions at high fugacity because of unusual crystallography (open tube lattice) compared to the traditional PdD unit cell (β-phase with its usual electron distribution). Traditional phases of metal hydrides (α and β) might not be unusual enough in structure, and electron distribution to support nuclear reactions; but SAV phases, distinct from β-phase and having open tubes and unfamiliar electron-proton (or deuteron) interaction, are insufficiently explored. Zhang and Alavi [26] have used density-function theory to show electronic structure is more important than entropy effect in forming SAV.

2. Analysis

The purposes of this section are to show: (1) these new phases, γ, δ, and δ', are equilibrium phases, (2) near room temperature, they require *creation* of vacancies by a mechanism other than diffusion (dragging of jogs by moving screw dislocations) and *relocation* of vacancies (aided by attraction to electromigrating D^+ ions), and lastly (3) apt incorporation into the Pd–isotopic hydrogen equilibrium phase diagram.

Although evidence for high vacancy content in SAV phases was originally obtained by unit cell dimensional changes [12], strongest evidence [15,20–24] for these three phases, with distinct crystal structures, comes from X-ray diffraction (XRD). It is also supported by thermal decomposition spectra [15,27,28]. In thermal desorption data

for pure Cu [27] and Ni [28], the spectra is the same for samples prepared via high-pressure/high-temperature to those created with electrodeposition (co-deposition of H(D) and Pd during electrolysis) at room temperature. In the former, the kinetics for formation is aided by high-pressure/high-temperature (high fugacity) while in the latter the structure is created atom by atom, so kinetics is bypassed, evolving directly into the lowest energy state, SAV. Only with subsequent thermal activation can hydrogen be coaxed into egressing (desorbed). The *kinetics* and signature of *desorption* is the same regardless of how the SAV state was arrived at.

A distinct unit cell constitutes a separate phase. It is shown from density functional perturbation theory (DFT) [15,29–36] that these new phases are equilibrium phases (lowest free energy), and as such, necessitate they be added to the Pd-D equilibrium phase diagram. Resistivity measurements (Section 4) link these phases, and a phase transition of δ to δ', to measured excess heat. These phases, occurring at high D/Pd ratios, offer unique pathways of open structure (vacancy tubes or channels, Section 5) with low resistance to electron and proton (and deuteron) transport.

SAV phases result from hydrogen-induced vacancy formation [15,20–24,29–36]. Vacancies have higher mobility (validated by DFT calculations [29–36]) from electromigrating D^+ which drag them for building SAV structures, (mechanism in Appendixes A and B). Higher numbers of vacancies are promoted by high dislocation density from plastic deformation, as outlined in Appendix B. These two steps in the formation of room temperature SAV would certainly limit nucleation and growth of δ and δ', but Sections 4 and 5 show that the volume fraction of SAV phases needed to support excess heat is an extremely small fraction.

On SAV Fukai [15] astutely recognized and stated:
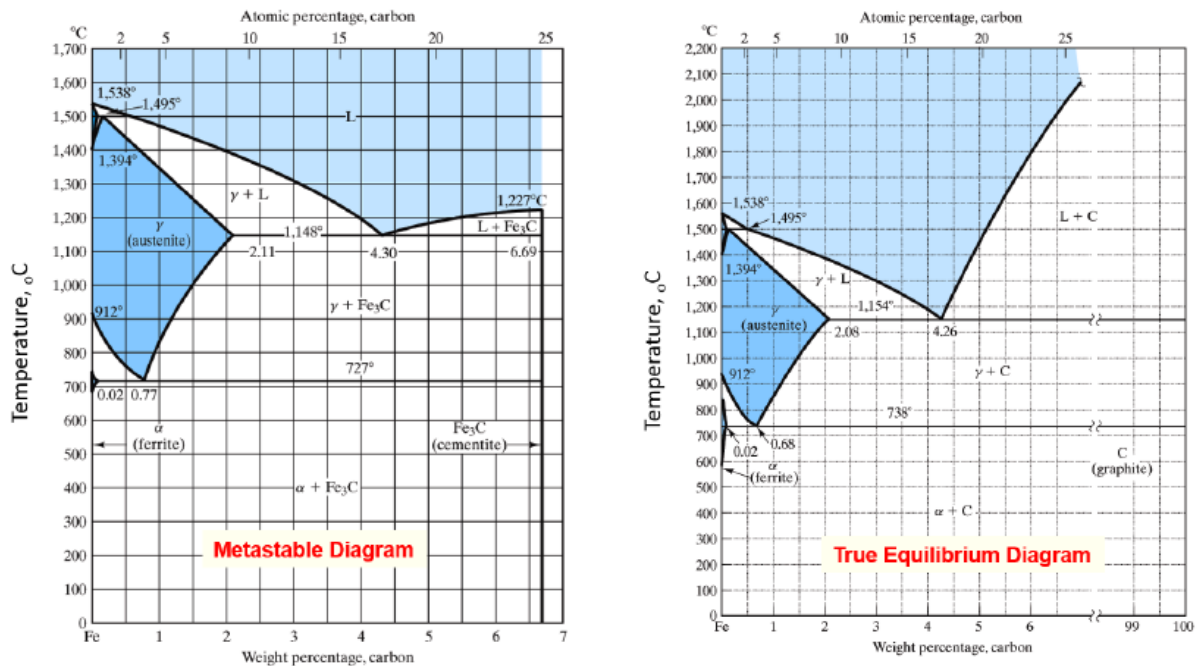
Figure 1. The Fe–Fe$_3$C (*left*) and Fe–C (*right*) phase diagram. The composition axis on the metastable diagram is weight % C (*left*) even though Fe$_3$C is a component (as opposed to C), whereas on the true equilibrium phase diagram, C is properly both composition axis and component; Fe$_3$C does not exist, adapted after [38].
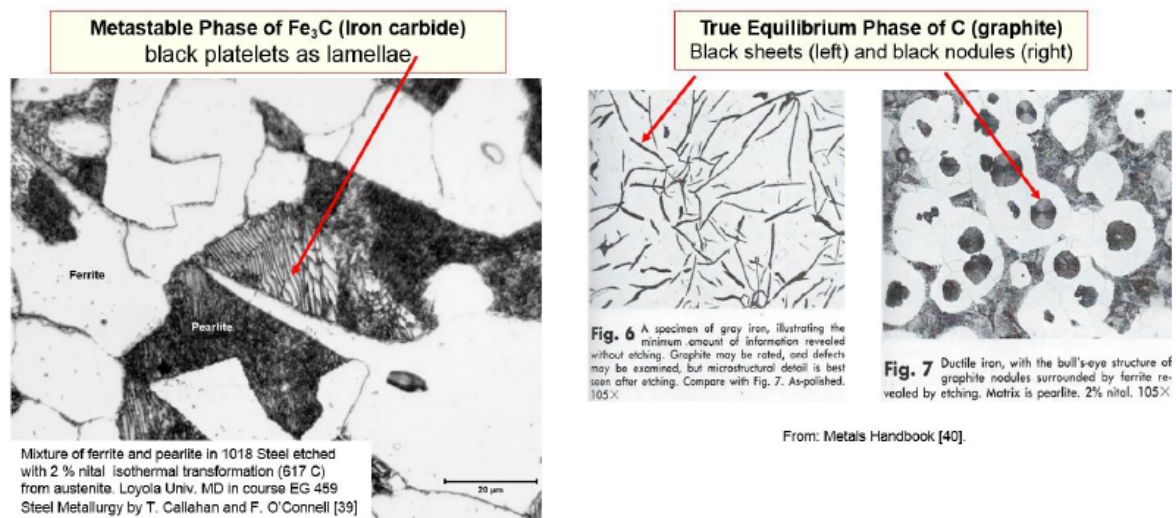
Figure 2. Micro-constituents for the diagrams in Fig. 1: those on the left (from [39]) are for the metastable Fe–-Fe$_3$C phase diagram, those on the right (from [40]) are for the true equilibrium Fe–-C diagram, showing that both types of diagrams are useful for steel and cast iron.

"... most important implication in the physics of SAV is that the most stable structure of all M–H alloys is in fact the defect structure containing a large number of M-atom vacancies. All M–H alloys should tend to assume such defect structures, ordered or disordered depending on the temperature, as long as the kinetics allows. In practice, however, M–H alloys are in most cases prepared under conditions where M-atom vacancies cannot be introduced. Thus it can be said that most (all) phase diagrams of M–H systems reported to date are metastable ones. These metastable diagrams are certainly useful as such, but the recognition that they are metastable ones is of basic importance. The real equilibrium phase diagrams including M-atom(s) vacancies have not been obtained so far."

Emending the phase diagram hinges on distinguishing between metastable and true equilibrium phase diagrams, as well as, the rules for possible and impossible phase diagrams. Okamoto and Massalski [37] express the relevant phase sequence rule: *There should be a two-phase field between two single-phase fields. Two single phases cannot touch except at a point.* Phase diagrams require 'necessary', but not 'sufficient' conditions, for presence of phases. The 'necessary' condition is the change in free energy must be negative ($\Delta F < 0$) for new phases to form. The 'sufficient' condition is from kinetics. In steel, both metastable and true equilibrium diagrams are useful since many heat treatments preclude equilibrium. The iron–iron carbide (metastable) and the true equilibrium phase diagram of iron–carbon are compared in Fig. 1 along with micro-constituents from each (Fig. 2). For Pd–isotopic hydrogen, the presently accepted diagram is metastable since some of the equilibrium SAV phases are absent because of kinetics. Traditional (historical) metastable diagrams of Pd–D(H) omitted SAV phases because they were only recently discovered. The equilibrium diagram with all phases of lowest free energy is presented below. Kinetics may also limit the size (volume percent) of phases in microconstituents. Kinetics for creation, mobilization and conglomeration of vacancies undoubtedly explain the incubation period to initiate excess heat in many low energy nuclear reaction (LENR) experiments

Figure 3 shows four isotherms (red) illustrating the phase sequence rule. In Fig. 4, from [36], one can see compliance and violation of the sequence rule in the V–H system. Figure 5 shows a violation of the phase sequence rule
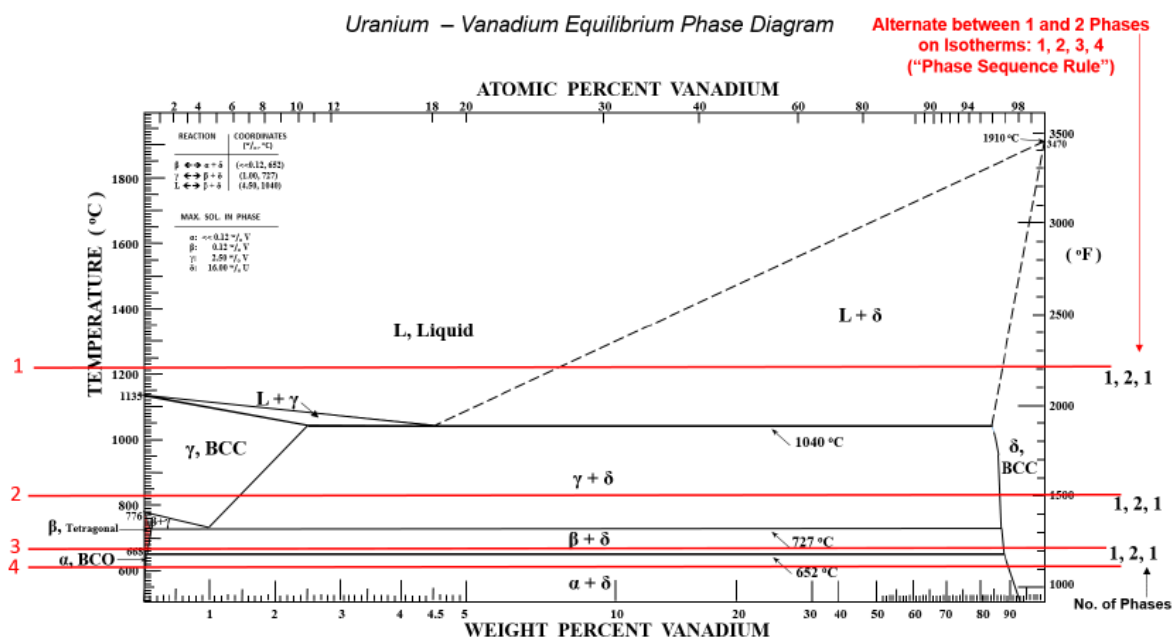
Figure 3. Phase diagram for vanadium–uranium system showing the phase sequence rule for four isotherms from [41].

in Pd–H [36]: the upward sloping phase boundary from D/Pd ratio of 0.66– $\sim$0.9 separating β from β'. A similar violation is in Fig. 5(B) from Araki et al. [42], but this can be corrected by interpreting their data as in Fig. 6 (red) to comply with the sequence rule, but necessitates a phase boundary at H/Pd ratio of 0.76 and another at 0.85 separating β from $\beta + \gamma$. In addition upward sloping red lines to the left of 0.76 and to the right of 0.85 have to be two-phase regions (curves with a nested two-phase field) as is shown below.

Figure 7 shows the unit cell for γ-phase (Pd$_7$VacD$_{6-8}$) from [22]. Delineation is revealed from two "unit FCC cells" (dark outline). From these, one sees the apposite true unit cell and superlattice structure of Pd$_7$VacD$_{6-8}$. D shifts slightly toward the corners allowing them to bind more to each vacancy. This is true for all of the D except the one in the central octahedral site not bound or trapped to any particular vacancy. Depending if this site is occupied, stoichiometric ratio of D to Pd is between 6 and 8 for 7 Pd atoms, giving D/Pd ratio between 0.857 and 1.143: γ-phase has mid-point stoichiometry D/Pd = 1 (subscript for D = 7).

Figure 8 combines the metastable diagram with SAV data to yield an equilibrium phase diagram. It has δ-phase Pd$_3$VacD$_4$, with D/Pd ratio 1.333 determined (see Appendixes C and D) from XRD [15–17,19,20,28,30,33,35] since there are 4 D for every 3 Pd at strict stoichiometry. These two phases (γ and δ) must, by the sequence rule, be separated by a two-phase field of ($\gamma + \delta$). The size of each phase field is determined as follows. The temperature extent has some uncertainty (dotted). The width of γ is based on the central interstitial site filling: empty in both half cells, filled in one of the two, or filled in both. For off-stoichiometry, the width of δ, from this analysis, is 1.333 $\pm$ the same width as the two-phase fields on either side of γ (.095 from Fig 8). This gives D/Pd$_{\text{Min}}$ = 1.33–0.095 = 1.24 and D/Pd$_{\text{Max}}$ = 1.33 +0.095 = 1.43. This construction follows Araki's et al. [42] data, indicating start and end of the two-phase region ($\beta + \gamma$) at 0.76 and 0.85 respectively. It is suggested that the two-phase region on the right of γ has the same width (0.095) from symmetry and a lack of data to support another value. This layout is qualitatively consistent with Fukai and Sugimoto [30,31] who specify two phases of different vacancy concentrations (named here γ and δ) and [20] who
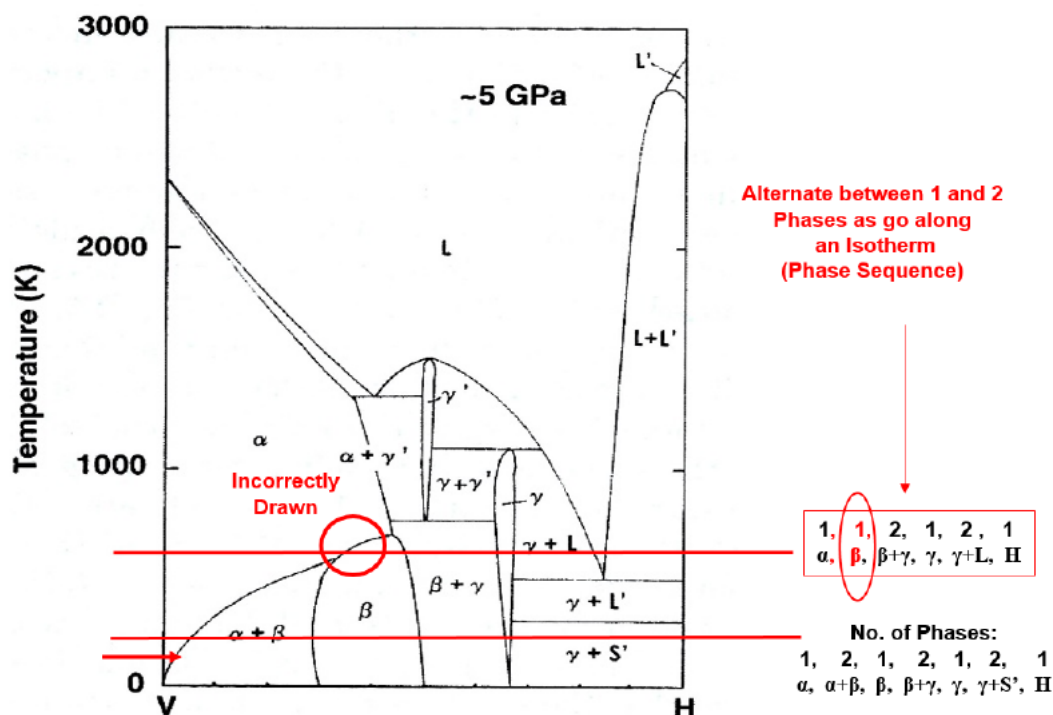
Figure 4.   Phase diagram for the vanadium–hydrogen system at 5 Gpa where the phase sequence rule is violated in the top isotherm but upheld in the lower isotherm, adapted after [36].

also show XRD evidence of two concentrations (12 and 20%). In the XRD work of Fukada et al. [22], these two phases were labeled moderate (0.86–1.14) and rich (1.24–1.43) vacancy concentrations.

There is also a δ' field, at D/Pd = 1.333 (Fig. 8). The difference between δ and δ' is D occupies octahedral sites in δ, while D occupies tetrahedral sites in δ'. The δ' appears below a temperature of 375 K based on resistivity data (Section 5), and is supported by tetrahedral occupancy by D from [23,24]. From DTF, Isaeva et al. [29] found, at lower temperatures, tetrahedral site occupancy by H (D) stabilizes SAV more than octahedral site occupancy. Neutron diffraction data of Ferguson et al. [24] and Pitt and Gray [23] show H migrates from octahedral to tetrahedral sites at lower temperatures.

The δ and δ'-phases are of interest to LENR. The δ''-phase has been in superconductivity literature and will not be detailed other than noting its existence and approximate position on the phase diagram. In addition, ε is not speculated on here other than its link to superconductivity at D/Pd ratio of 1.6 as Tripodi et al. [43] have predicted. In summary, SAV phases (γ, δ, and δ') are equilibrium phases, require creation and mobilization of vacancies, and are incorporated into the Pd–isotopic hydrogen equilibrium phase diagram.

3.   Materials and Experimental Procedure

Unalloyed Pd from Johnson–Matthey was used as 0.5 mm diameter rod of length 25.4 mm in an electrolytic cell with Cu leads connected to the current-controlled DC power supply. The specimen diameter was chosen consistent with results of electromigration analysis for D^+ (Appendix A). Since Pd has a much higher melting point than Cu,
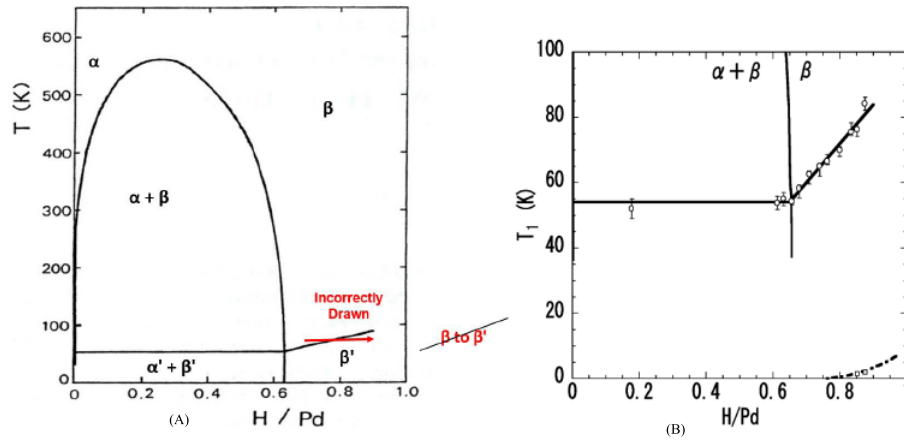
Figure 5. (A) The Pd–H phase diagram with the phase sequence rule violated. This diagram is a metastable diagram lacking equilibrium phases (γ,δ, and δ'), adapted after [36]. (B) A portion of the Pd–H phase diagram of Araki et al. [42] with the phase sequence rule violated. Open circles and open squares are from measurements in their work. This diagram is a metastable diagram lacking equilibrium phases (γ,δ, and δ'), after [42].

attachment was completed as in Fig. 9 by heating tips of 5.19 mm diameter (#4 gauge wire) copper leads with a torch to form a molten bead, inserting the end of the cold Pd specimen into the droplet, while withdrawing the flame,
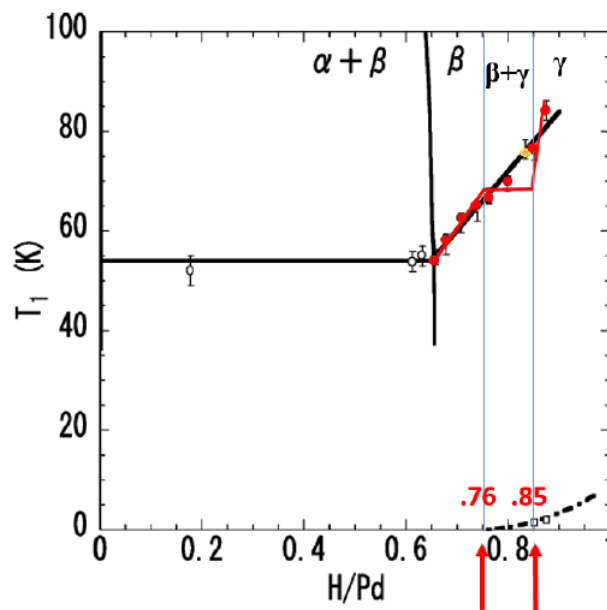

Figure 6. A portion of the Pd–H phase diagram of Araki et al. [42] with red lines being another interpretation of phase boundaries. Open circles and open squares are from measurements in their work. This diagram is also a metastable diagram lacking equilibrium phases (δ and δ'). Adapted after [42].
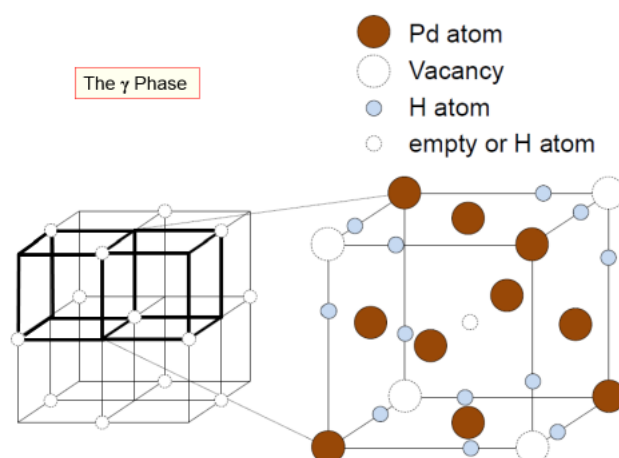
Figure 7. Superlattice structure of Pd_7VacD_{6-8}. *Left*: super-cell lattice showing only vacancies. *Right*: half-cell structure magnified from the super-cell with heavy lines. The H-atom at the body center does not bind to any vacancy, thus the subscript for hydrogen varies within a range from 6 to 8. Adapted from [22].

causing instant solidification of Cu, braze-bonded around the end of the Pd specimen. The Pd remained solid due to higher melting point. This method was used on both ends of the Pd forming a good electrical connection for the cell. It allowed for current to be driven through the Pd independent of electrolysis current from platinum (Pt) anode to Pd cathode. It was also used for Pt specimens in Pt/H_2O control cells. Expansion of Pd during absorption of D was accommodated by high ductility Cu preserving the bond for the lifetime of the experiment. Contact of electrolyte with Cu leads, was avoided by heat shrink electrical insulation tubes and then sealing Pd ends (Fig. 10) with miccrostop
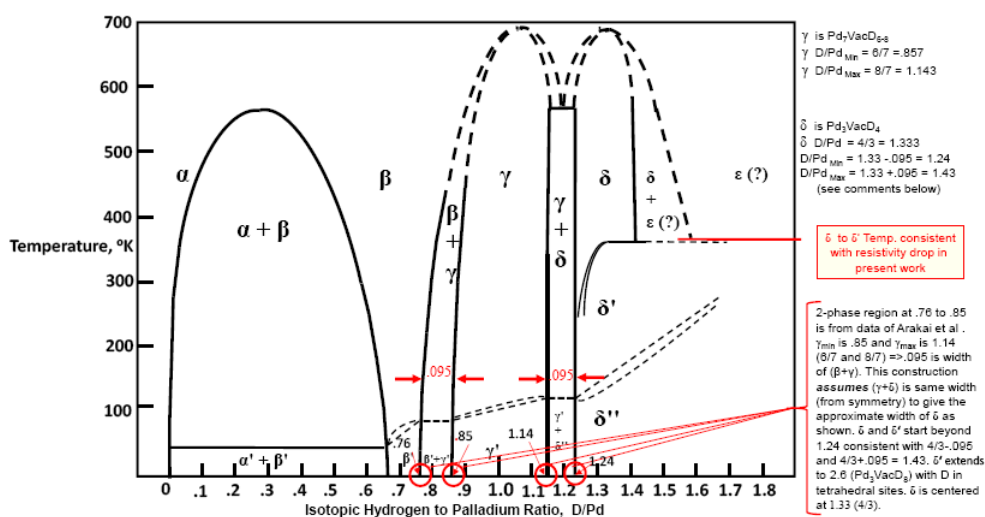
Figure 8. Equilibrium phase diagram for isotopic hydrogen–palladium.
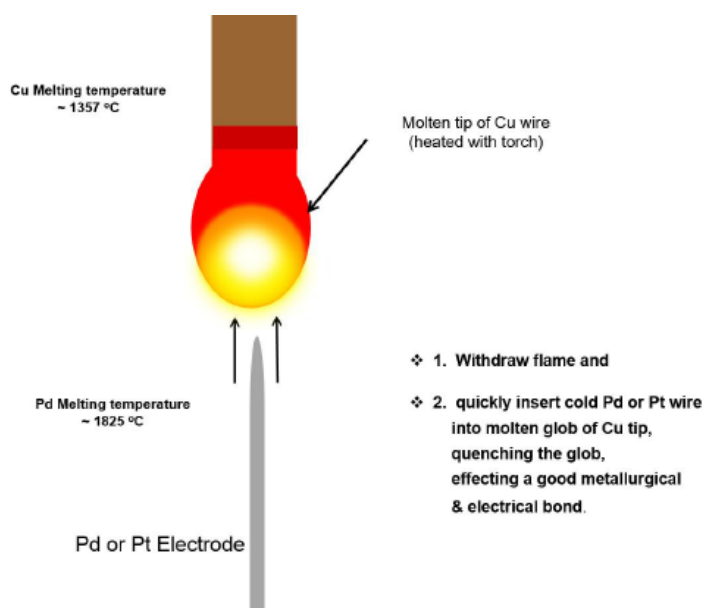
Figure 9. Method of preparing and attaching Cu leads to Pd or Pt cathodes.

stop-off lacquer (such as MICCROSHIELD Stop-Off Lacquer from Tolber Division Miccro-Products).

The electrolyte was 18.0 ml of 0.5 mol LiOD in 99.8% deuterium oxide D_2O from Cambridge Isotope Laboratory. The cells were constructed by nesting four slightly different size Pyrex test tubes, each separated by two O-rings and a thin air space. A Teflon top, sealed with O-ring, excluded ambient atmosphere by allowing the positive pressure of O_2 and D_2 gas to exit through a capillary tube into a reservoir of vacuum pump oil. This arrangement is shown in Figs. 11–13. Fleischmann and Miles [44] showed recombination is either zero or too small to be a source of heat. There was visual monitoring of cell electrolyte level and exit gasses. This configuration of four-nested tubes reduced overall heat transfer from the inner test tube and increased sensitivity (producing a larger delta Temperature, ΔT, for each input watt). Cells were calibrated by measuring the power in and ΔT, the difference between cell temperature and surrounding air temperature inside the calorimeter. Power from electromigration current (current-control mode)
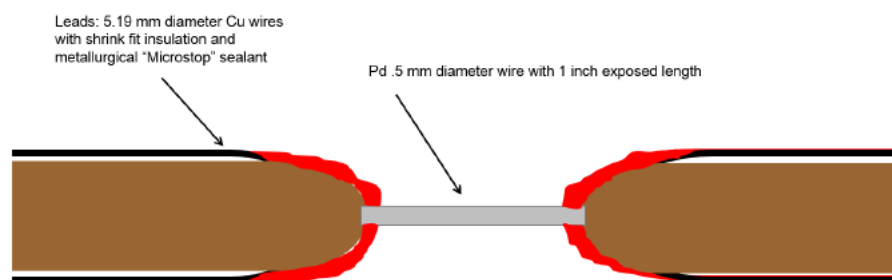

Figure 10. Pd or Pt (control) cathodes with brazed electrical leads of Cu isolated from the electrolyte in the cells by heat shrink tubes and Microstop lacquer sealant.
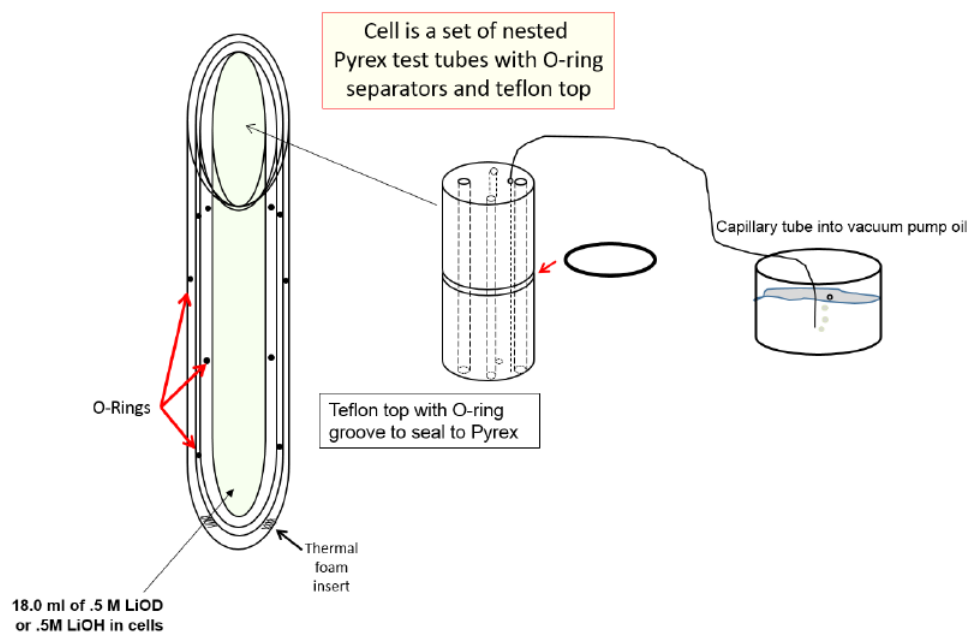
Figure 11. Electrolytic cells constructed by nesting four Pyrex test tubes (with O-rings) and Teflon top, through which cathode, two cathode leads (Cu), anode lead (Pt), two small Pyrex tubes (two) for thermocouples, make-up water from syringe, and exit gas tube come through. Top of cell is distorted in drawing which is not drawn to scale.
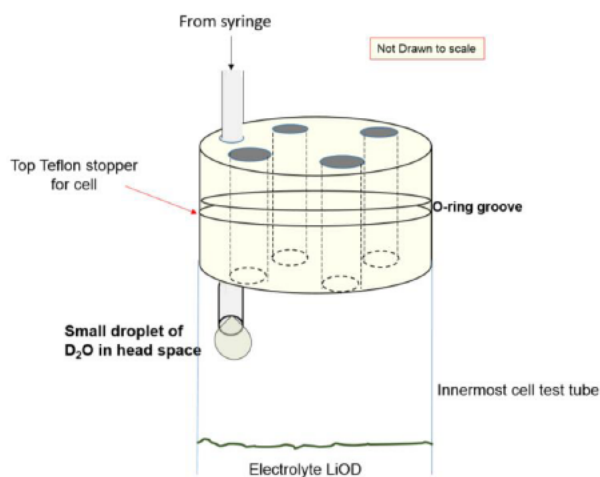
Figure 12. Suspension of D_2O or H_2O droplet from make-up water syringe tube in the head space above electrolyte allowed growth and thermal equilibration before dropping into the electrolyte. Typically this took about 10 min, depending on electrolysis current to which the delivery rate was matched.
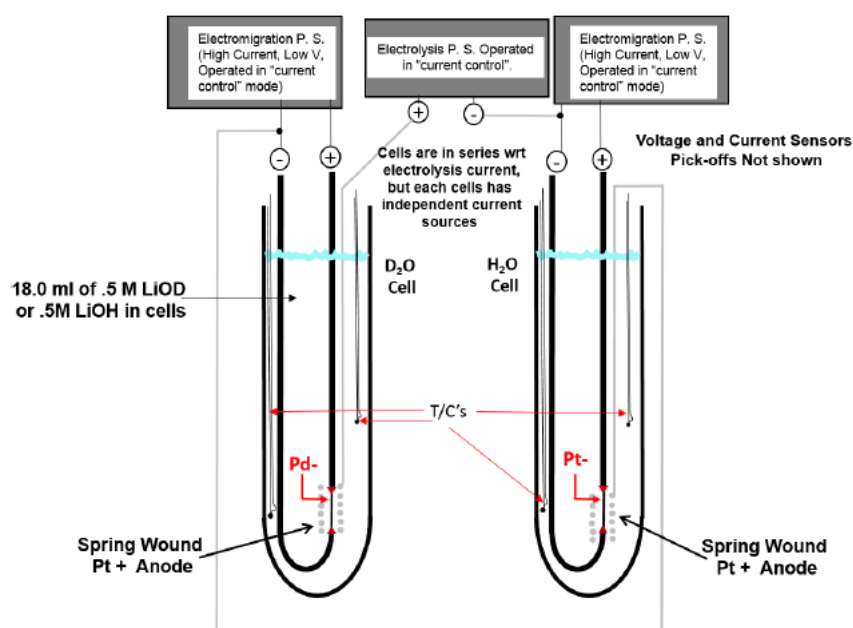
Figure 13. Electrolytic cells of four nested (not shown) Pyrex test tubes, sealed with Teflon tops (not shown). Both cells are in series on one current controlled power supply (PS). Independent electromigration currents from PS's for each cell were also operated in current control mode.

through Pd specimens was the product of current times voltage drop along the Pd specimen. This voltage drop was measured outside the cell on the Cu leads carrying electromigration current since 98.6% of the drop occurred in the PdD portion because its resistivity is higher than Cu (5.9–11.8 times higher depending on D loading), but most importantly because of its greatly reduced cross-section (ratio of Cu area to PdD area $= d_{Cu}^2/d_{Pd}^2 = 108$). The net effect of these two factors, along with the ratio of Cu to Pd lengths, is the ratio of voltage drop in PdD to that of the Cu leads. It is 69.4 to 1. This assessment includes the length of Cu (into and out of the cell) of 35 cm and the average of least and most resistivity values. Power-in for the electrolysis portion (current-control mode) was electrolytic current times electrolytic voltage minus thermoneutral potential (conservative values of 1.52 V for D_2O and 1.48 V for H_2O were used). Cell temperature was obtained from thermocouples placed inside two capillary tubes in each cell (Fig. 13). These were averaged with each other and over time (collected every 0.01 s yielding 5000 measurements, and were averaged for each temperature or voltage collected, giving an output data set every 15 min). Thermocouples were welded and their output voltage compared to a standard thermocouple calibrated periodically at the National Institute of Standards and Technology, assuring absolute accuracy within 0.05°C for Temperature readings after extensive averaging (5000 readings). It should be noted that precision for any given thermocouple was better than 0.05°C since repeatability on the same thermocouple did not include an offset (systematic error) normally involved when measuring absolute accuracy.

A calibration curve of ΔT versus power-in was run for cells with 1–4 nested tubes in an effort to assess sensitivity by adding tubes. This was motivated by the small volume of Pd electrode, anticipated power density releases (W/cm^3), and a desire to distinguish between chemical energy (a few eV/atom) and nuclear energy (between keV/atom and MeV/atom, depending on the fraction of atoms participating, see Section 4). The sensitivity increased with each nesting Pyrex tube and its associated dead air space.

Maintaining electrolyte level in cells used a Harvard Apparatus Model 22 Digital Syringe Pump outfitted with two syringes, one with heavy water from Cambridge Isotope with 99.8% D and one with double distilled light water. The selectable rate of delivery (between 0.002 μl/h and 55 ml/min) was established by developing a table of instrument input settings for each electrolysis current. Make-up heavy and light water in the form of small droplets dangled in the cell head space (lasting about 10 min) before dropping into the electrolyte (Fig. 12) and allowed for thermal equilibration. Use of the syringe pump (slow but constant rate of delivery) eliminated thermal shock when replenishing D_2O and H_2O. Thermal shocks (negative temperature spikes) had been a shortcoming in this field. Sudden large additions had additional surface area for heat transfer and cooler electrolyte mass for a given power level and upset excess heat reactions. The effect of over or under filling of electrolyte (eliminated with correct syringe pump settings) is shown in Section 4. The time constant was determined for the heavy water cell to be about 34.5 min by the standard method of determining a time constant (Fig. 14). It is compared to one of about 116 h for the entire calorimeter chamber (202 times larger). This insured a small but distinctive power spike in the cell could be measured since chamber temperature was constant and capable of absorbing the power of the cells without any change in overall calorimeter temperature (the heat capacity of the calorimeter was 2500 times higher than that of the cell). With the ratio of thermal diffusivity ($\alpha = k/(\rho\ c_p)$) of air to water at 150 ($\alpha_{air}/\alpha_{water} \approx 150$), the temperature inside the chamber was equilibrated and constant more consistently than using a commonly employed water bath. Here k is thermal conductivity, ρ density and c_p is constant pressure heat capacity. There was no forced air velocity inside the
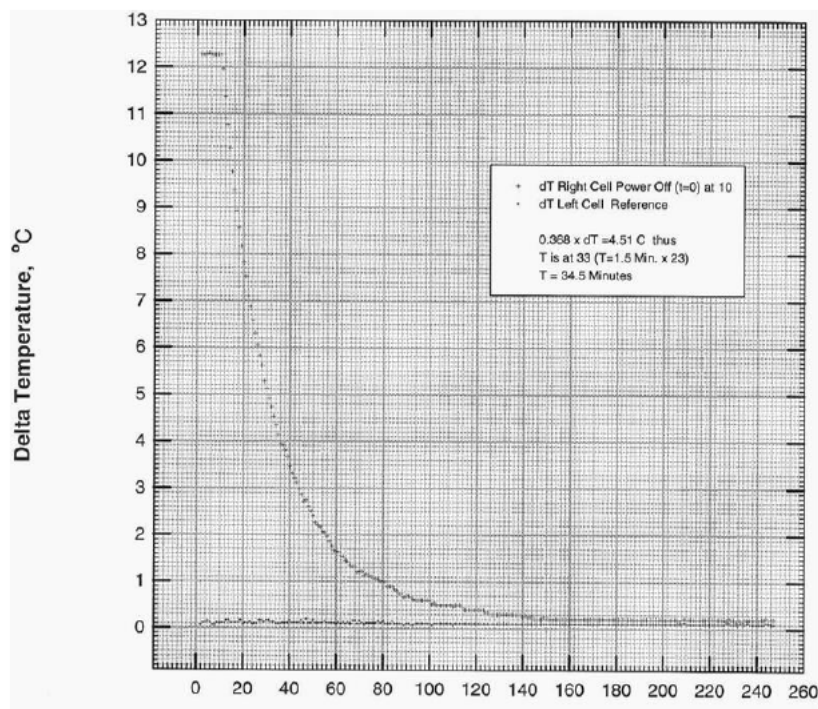
Figure 14. Time constant determined for right and left cell (*right shown*) in the constant temperature chamber to be 34.5 min. The constant temperature chamber was measured at approximately 116 h (about 202 times longer while the heat capacity was 2500 × higher). The time constant τ represents the time for it takes the cell's step response to reach $1-1/e$ ($\approx 63.2\%$) of its final (*asymptotic*) value.
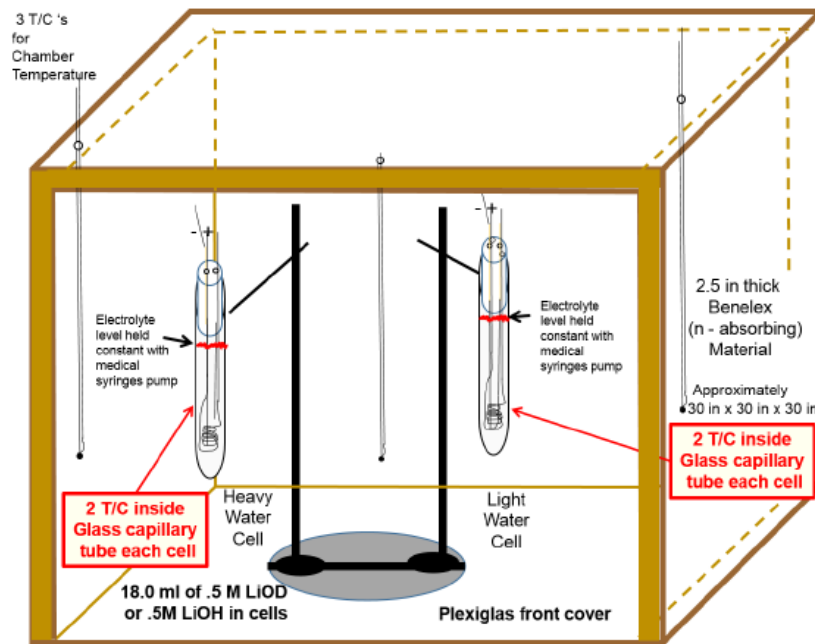
Figure 15. Constant temperature chamber with thermal time constants: τ chamber $\gg \tau$ cells.

calorimeter, only natural convection.

The calorimeter itself (Fig. 15) consisted of a chamber approximately 75 cm $\times$ 75 cm $\times$ 75 cm with wall thickness of 6.4 cm of Benelex (pressed fibers board) surrounding cells on all sides except the front, which had Plexiglas for visual monitoring the cells, especially electrolyte level. Three thermocouples, inside the chamber were averaged for calorimeter media temperature. There was never any difference in these three readings (within precision), however, averaging improved reliability and confirmed lack of forced convection.

A data acquisition processor card 2400a by Microstar Laboratories Inc. was used for all data acquisition of voltages, and currents (measured as a voltage drop across a precision resistor) for power input, and for thermocouple readings. Precision, using extensive averaging, for the power-in was $\pm$ 0.0005 W, while that of the ΔT was $\pm$ 0.05°C (or better as explained above) and that of power-out of $\pm$ 0.015 W (based on the limiting value of ΔT of $\pm$ 0.05°C). This gives an overall precision for the experiment of $\pm$ 0.5%, enabled by: (1) Use of the data acquisition card, eliminating human bias and giving large averaged data sets. (2) Use of the calorimeter chamber, with time constant over 200 times larger than that of the cell. (3) Use of the syringe pump eliminating shock and maintaining constant level. Other factors that contributed to successful excess heat production were preconditioning the Pd to a high vacancy and dislocation density by anodically unloading and cathodically re-loading (back over resistive hump and over again) four times at low current density ($<$50 mA/cm^2) before measuring heat (Appendix B), and selecting the diameter of specimen to promote electromigration of D$^+$ without adding significant resistive parasitic power (Appendix A). The D/Pd ratio increased with each loading cycle: four cycles were found to be an optimal number. Electromigration promotes concentration enhancement at the bottom end of the Pd, and causes redistribution of vacancies. Using plastic deformation, with a high dislocation density, is suggested by Sugeno and Kowaka [45] and Lewis [46] in Fig. 16. The final hardness (and dislocation density), from hydrogen insertion and removal into well-annealed Pd, is the same as
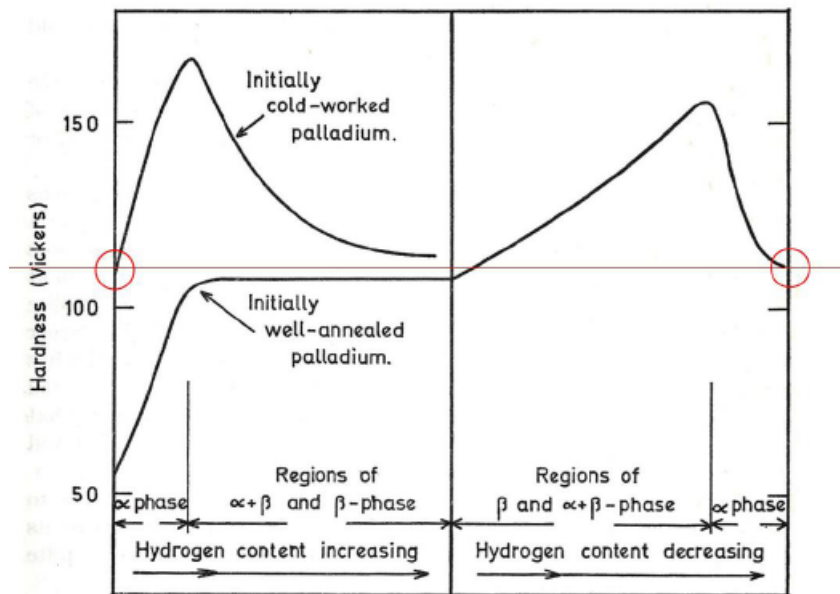
Figure 16. Hardness as a function of hydrogen content during insertion and removal of hydrogen at 25°C after [45,46]. The final hardness (and flow stress τ) and dislocation density ρ from insertion and removal of hydrogen into well-annealed Pd have the same starting values as cold worked Pd. Hardness (flow stress) are related to dislocation cell size d and dislocation density ρ as shown by Holt [47] and Staker and Holt [48]: $\tau = Kd^{-1}$, $d = 16\rho^{-1/2}$, $\tau = 0.57\,Gb\rho^{1/2}$, where G is shear modulus, b Burgers vector.

the starting value of cold worked Pd. Dislocation intersections create dislocation jogs and enables vacancy creation in bulk without need for diffusion from surface or grain boundaries. Hardness and flow stress are measures of dislocation density and dislocation cell size, as shown by Holt [47], Staker and Holt [48], and Kuhlmann-Wilsdorf [49]. Deutges et al. [50] have shown, by transmission electron microscopy that cell formation, common to most metals, also occurs in PdH and results in higher diffusivity of H, consistent with higher vacancy concentration (Appendix B).

This method utilized the Fleischmann–Pons cell except for four-wire leads and three power supplies. In-situ resistance monitoring of D to Pd ratio after Burger et al. [51] and McKubre et al. [52] ensured loading over the resistive hump (D/Pd = 0.74) to higher values of D/Pd (0.93), and monitored changes in resistance after excess heat initiated. Their analysis of variation of resistivity ratio $\rho_\beta/\rho_{\mathrm{Pd}}$ with r_x (the D/Pd ratio) showed ρ_β follows the relationship: $\rho_\beta/\rho_{\mathrm{Pd}} = 0.97869 + 3.0001(r_x) - 15.090\,(r_x)^2 + 44.155(r_x)^3 - 49.119\,(r_x)^4 + 17.577(r_x)^5$, with $R^2 = 0.999$. Thus by measuring the initial (ρ_{Pd}) and in situ (ρ_β) resistances D/Pd ratio as r_x in this equation was determined and constantly monitored at all times. Once crossing the maximum (hump) at D/Pd = 0.74, one could be confident of the loading ratio as long as resistivity ratio ($\rho_\beta/\rho_{\mathrm{Pd}}$) never rose above the maximum value (2.004) during a run (never crossed back over the hump by de-loading). Rising and falling resistivity values were observed and monitored during electrolysis potential reversals while crossing the miscibility gap four times.

Previous LENR research bid to avoid loading hydrogen and its isotopes through the α to β miscibility gap. This scheme was initiated by the industry using Pd and Pd–Ag alloys for purification of hydrogen and isotope separation. The main concern was to avoid damage to Pd or Pd–Ag alloys, anxious about structural integrity (resistance to fracture). This damage is due to deformation and cracking accompanying large volume change associated with α to β-phase change. It progresses from sever plastic deformation (high dislocation density but unfractured) to eventually exhausting

the limit of ductility culminating in cracks. Whether plastic deformation leads to cracking or continues to even larger amounts of deformation depends on the state of stress (a combination of tensile and shear versus compressive and shear). Motion of dislocations (plastic deformation) is attained only by shear (not compressive or tensile) stress, whereas fracture is initiated by tensile stress. The motivation for the use of the protocol of loading and unload hydrogen four times by reversing the electrolysis current is to create a high dislocation density with copious intersections with screw dislocations in dislocation cell walls. These generate vacancies (by the mechanism in Appendix B) and are caused to migrate to unit cells that become ordered SAV unit cells (δ and δ' phases by the mechanism in Appendix A). These unit cells grow to form small islands of multiple unit cells (see Sections 5 and Appendix B) that constitute a volume fraction near 0.03 % (for δ-phase). The way to avoid fracture is to assure that the state of stress minimizes tensile stress. This state of stress, displayed on Mohr's circle, would be shifted as far left (into negative compressive stress) as possible but with a large diameter (high shear stress). In this research, creation of dislocations and their intersections by loading and unloading four times created vacancies with the beneficial side effect of increasing the diffusion rate for hydrogen (of course even much higher diffusion rates are provided within SAV unit cells as they grow in size). If fracture occurs, high loading rates are not possible, so loading slowly in the beginning effects the state
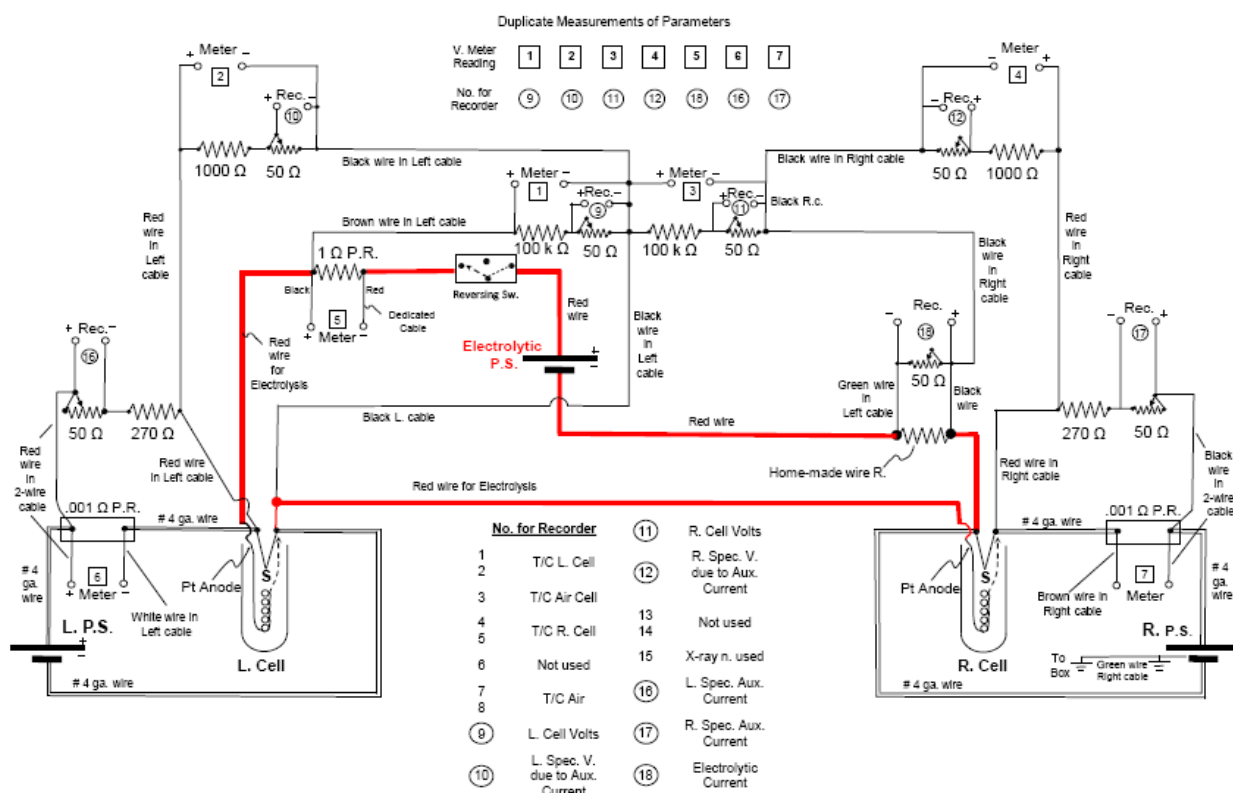
Figure 17. The wiring diagram using three power supplies (PS). The numbers in boxs or circles are locations of readouts (meter and recorder are redundant for data acquisition processor card). Pd and Pt cathodes, S, are connected to 5.19 mm diameter Cu leads, labeled #4 ga. wire, and the electromigration current there in is labeled Aux. Current. The Pd/D$_2$O and Pt/H$_2$O are labeled L. cell and R. cell, respectively. Three types of wires are indicated: double line (electromigration circuit), red line (PS for electrolysis with cells in series), and light black lines to data read-outs.

of stress minimizing tensile stresses between regions highly loaded (expanded) and those not yet loaded, as indicated by Cravens [53] and leading to the optimal number of loading/de-loading/reloading cycles of four.

Electromigration was incorporated for monitoring resistance (measuring the voltage drop along the length of Pd) and D/Pd ratio, and to force movement of D^+ ions toward the bottom of the specimen. Because of attraction of vacancies for D^+ ions, it also promoted concentration of vacancies, easing activation energy of SAV. It also balanced the power with a small amount of resistive heating in either light or heavy water cells. They were in series for electrolysis, but electromigration currents were controlled independently.

Figure 13 shows heavy water Pd and light water Pt cells wired in series (same current). The Pt anode was wound as tightly as possible to the cathode, lowering electrolysis voltage and power-in. Use of 0.5 M LiOD and 0.5 M LiOH also reduced power, providing a more sensitive calorimeter. Two thermocouples inside small capillary tubes monitored cell temperature. They were averaged for each cell. Complete wiring diagram for the electrolysis, electromigration, power supplies, reversing switch, precision resisters for currents, other voltage divider resistors for readouts, and locations for the data acquisition processor card tapping are shown in Fig. 17. The numbers in a box or circle are locations of these readouts. The Pd/D_2O cell and Pt/H_2O cell cathodes, marked S, are directly connected to the 5.19 mm diameter Cu leads (labeled #4ga. wire) and to the power supply (PS). The electromigration current is labeled Aux. Current in Fig. 17.

In Fig. 18 there are three hypothetical data sets of ΔT versus power-in, where the *accuracy* (red line) can be improved by adding more data. However the *precision* cannot be improved unless methods are taken to reduce the sources of error in ΔT as described above. This kind of scatter of green data points from the red line is too great in the left figure to provide confidence that any given green point is a result of excess heat. The second hypothetical data set (center) has improved precision but with same accuracy. The right data set has precision and accuracy to measure excess heat for a given specimen size (more excess heat for a larger size).

In developing calibration curves for light and heavy water cells, data were taken either before loading to high ratios or by using a Pt cathode and Pt anode. Data (with 5000 readings) were averaged by the data acquisition card and associated computer software at 15 min intervals from all thermocouples, voltages and currents, filled a file without human intervention, and then plotted as small dots. By changing electrolysis and/or electromigration current slightly
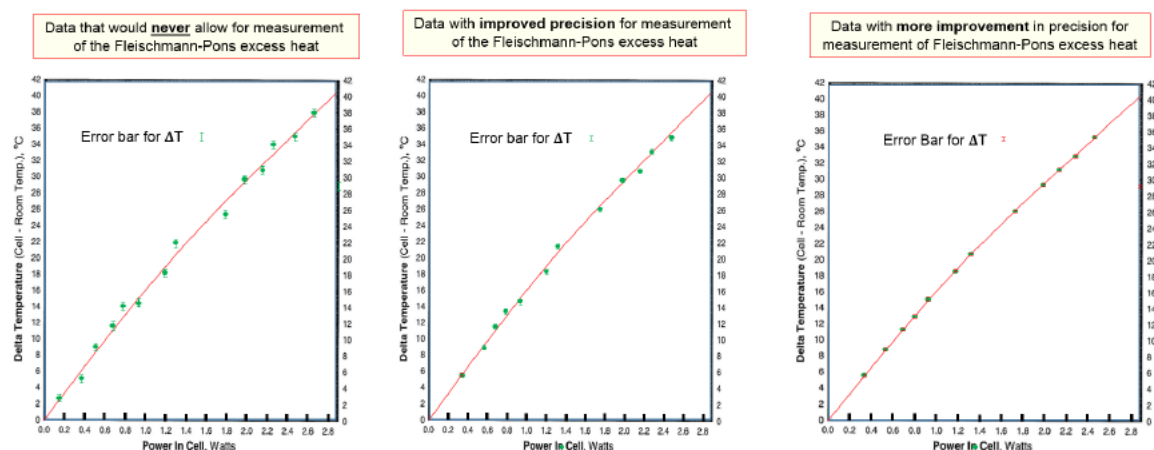

Figure 18. Hypothetical data of ΔT versus power-in, where the *accuracy* (*red line*) can be improved by adding more data to the set, but improvement in *precision* requires other means.

to new settings, data was acquired at new positions on the graph (about every 45 min): this permitted closely spaced values which filled in the entire line (*curve of dots*).

4. Results

Figure 19 shows a calibration curve for ΔT versus power-in with ΔT measured in degrees Celsius and power-in measured in watts obtained as just described (Section 3). It uses a small dot as the data character symbol: there is no additional curve through the data. This demonstrates higher precision than that reported above of ΔT of $\pm 0.05°$C. Figure 20 shows the same data with a calibration check (data characters of crosses, $+$) added after 46 days. These crosses are plotted with larger font size to distinguish them from the dots, nonetheless, the centers of the crosses fall on top of the original calibration, indicating no shift in calibration.

Figure 21 shows the calibration curve drawn with a line (replacing the dots) and extended to higher power-in levels. The ΔT and power-in are during operation of the Pd/D$_2$O cell at various times during the 46 days of operation. A straight line at higher levels of power is a conservative estimate of the calibration curve since it is slightly concave down (slightly lower than shown). There are rare scattered data below and above the calibration curve. All the data below calibration were taken by the data acquisition processor card under non-equilibrium conditions: either by a deliberate attempt to document the effect of cell overfilling (raising the electrolyte level above equilibrium operating level of 18.0 ml) or when electrolysis was deliberately stopped briefly, allowing the cell to cool below equilibrium calibration conditions. These periods are not part of calibration or equilibrium conditions (normal operation of the cell). The
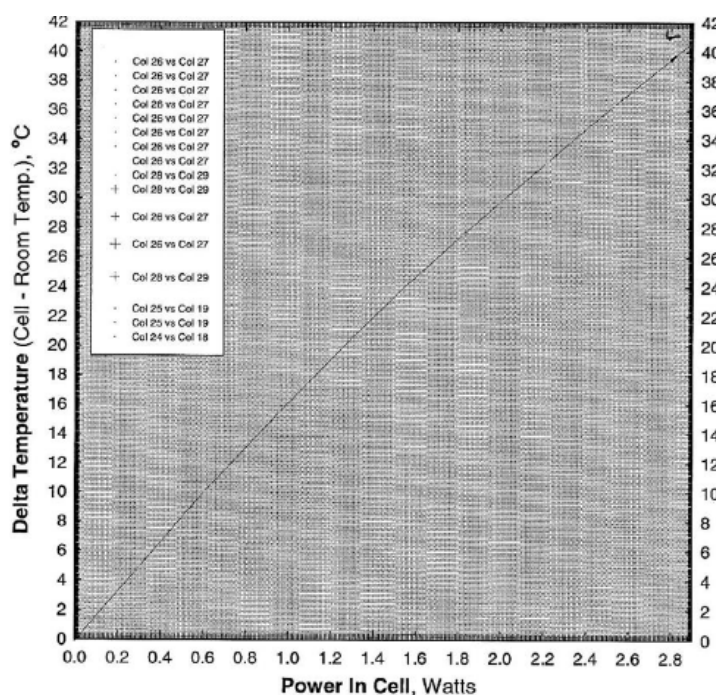
Figure 19. Calibration curve of right cell (Pt/Pt) and left cell (Pd/Pt). The line is a series of small dots closely spaced determined from data acquisition card and computer data readings from Fig. 17, for plotting without human intervention. Precision is as follows: Power In $= \pm$ 0.0005 W; $\Delta T = \pm 0.05°$C; Power Out $= \pm 0.015$ W; Over all Precision $= \pm 0.5\%$.
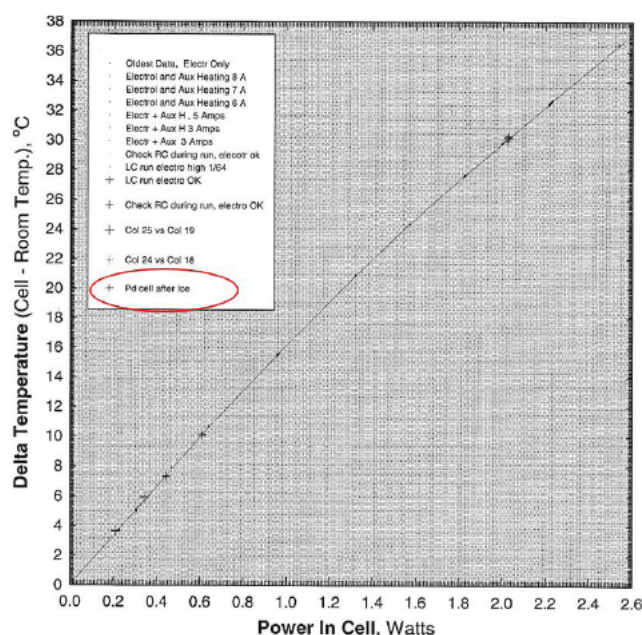
Figure 20. Calibration curve of right cell (Pt/Pt) and left cell (Pd/Pt) *before* electrolytically loading D, dots (·) and *after* ice-quenching the Pd (*left*) cell (*crosses*, +), stopping excess heat 46 days later. Small dots forming line are from voltages, currents and thermocouples inside cells and outside cells in calorimeter chamber. Crosses and dots on same curve proves no shift in the calibration. Data acquired and plotted without human intervention. Precision is as in Fig. 19.

clustered data set at the left and below the line near power-in of 2.85 W is the result of deliberately overfilling the cell by about 1.5 mm from the equilibrium calibration mark, then allowing the electrolysis to run without the syringe pump filling (pump off). At the point where the data characters (small crosses) meet the calibration line, the electrolyte level met the equilibrium level mark of 18.0 ml. This behavior was tested again at 3.29 W (tight cluster) with about 1 mm overfill and then allowing electrolysis to run until a 1 mm under-fill condition (data above the line).

All other data (crosses) above calibration line are a result of excess power, ranging from 0.10 W (about 4.7% of power-in, depending on power-in) to 0.32 W (9.6%). Excess power stayed in this range most of the 46 days, except for two events of run-away power that required cutting back power-in to prevent boiling of the cell. They are shown in Fig. 22. Excess power during run-away was triggered by an increase in electrolysis current. Before run-away, the light water and heavy water cell were matched in input power by trimming the electromigration current. The fact that the heavy water cell was higher in temperature by about 2.5°C shows it was producing excess power. When electrolysis current was increased from 444 to 535 mA and the control cell (light water) was again matched in power, the temperature of the heavy water cell started to run-away necessitating a cut back in current to 435 mA; but excess power continued. With only a modest increase in current (from 435 to 442 mA), temperature ramped into run-away again, but stabilized in the 82°C range, considerable higher than 67°C, prior. This second run-away event produced 2.4 W with 1.2 W input. Total excess *heat* (excess energy) over a 46 day period of 0.775 MJ or 150 MJ/cm^3 of Pd or 14 000 eV/Pd atom was from integrating the suitable power values over this period. This is of such a magnitude that it must be a nuclear reaction; but there is no evidence in this study which nuclear reaction.

In this study seven Pd specimens were run. Six specimens gave excess *power*. Two gave extensive excess *heat*
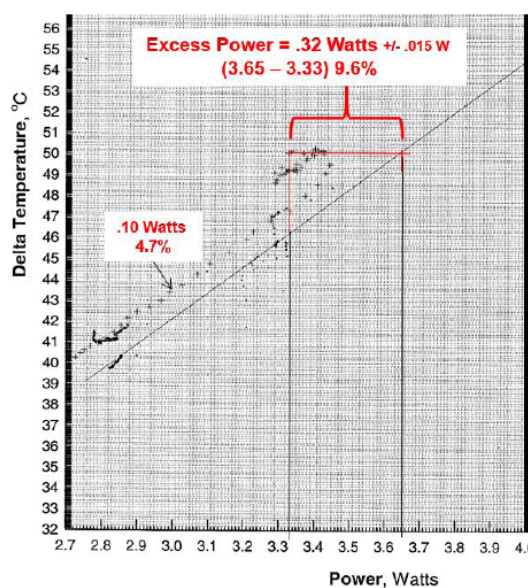
Figure 21. Left cell (Pd/Pt) in D_2O exhibiting excess power (*crosses*, +). The line is drawn through the calibration curves of Figs. 18 and 19 (without excess heat). Watts of excess power are above the calibration curve but varied for the entire 46 day period as shown by periods of 0.10 and 0.32 W excess power.
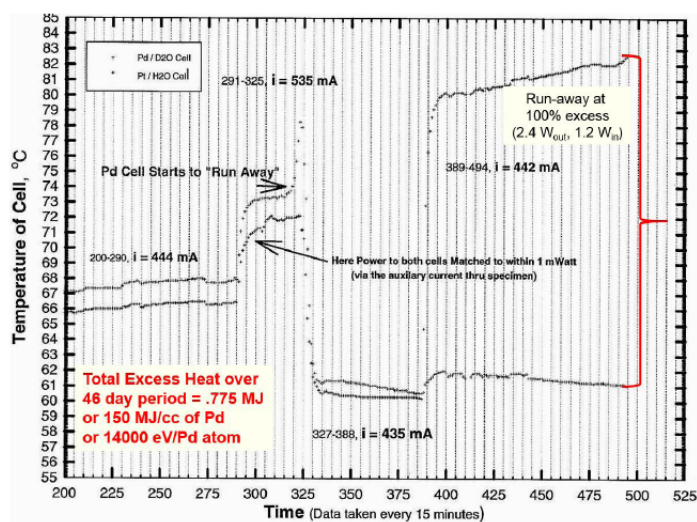
Figure 22. Left cell (Pd/Pt) in D_2O exhibiting excess power (+) and responding to sudden changes in electrolytic current. The temperature of both heavy and light water cells are shown as a function of time (data acquired every 15 min). Before initiation of run-away events, power to both cells was matched to within 1 mW.
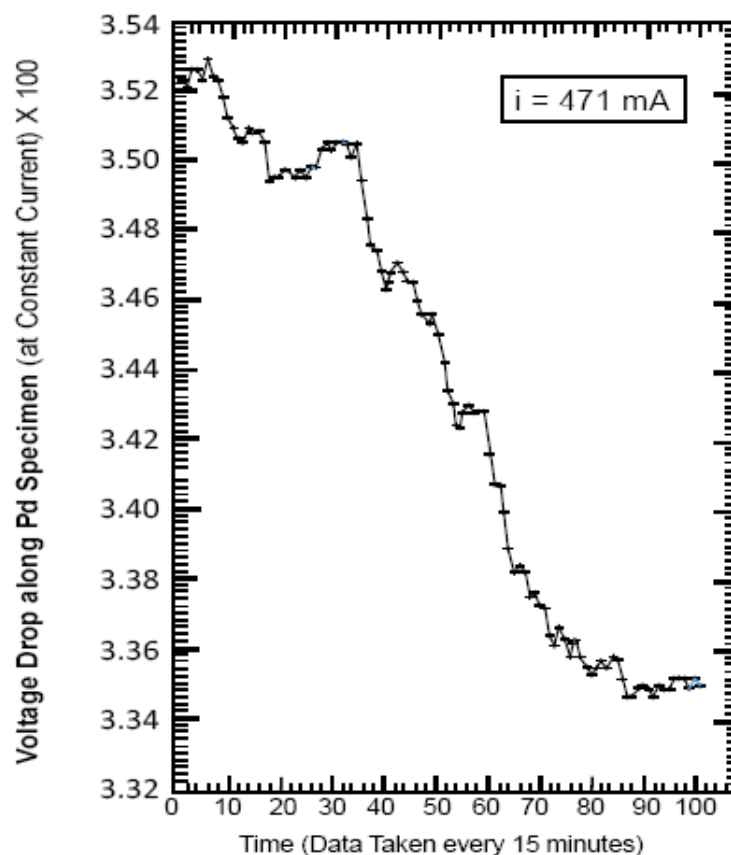
Figure 23. Left cell (Pd/Pt) in D_2O exhibiting excess power (+). The resistivity of the PdD had gone over the hump in resistance (near D/Pd = 0.74) at the beginning of the run assuring spec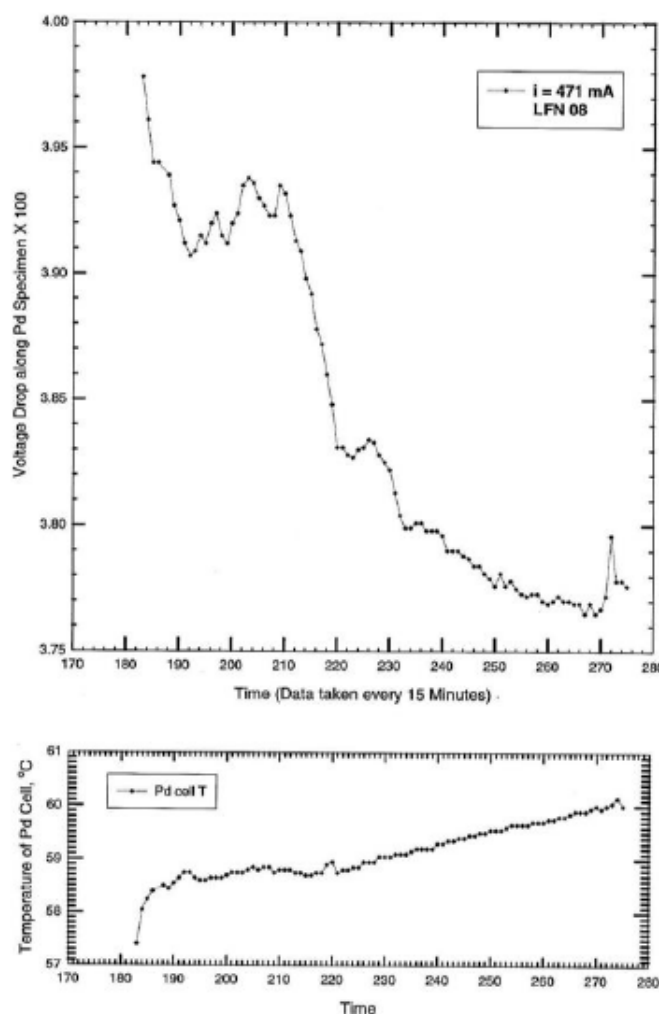imen is in the range above an average D/Pd = 0.93 for the events featured here. The drop in voltage along specimen is from a change in its resistivity since electromigration current is constant and the temperature of the cell is increasing.

similar to that reported. The ones that gave excess power (but not excess heat) were deliberately stopped for various reasons not associated with excess heat–not run long enough to determine excess heat that exceeds the limits of chemistry. It is reasonable that they would have given excess heat. Another specimen (seventh) had a visible crack, no excess heat, and did not load properly. It was run however to verify the importance of loading on excess heat.

Another important observation was the change in resistivity during excess heat in Fig. 23. Resistivity is measured as a drop in voltage along the Pd with constant current. Each number on the time scale is 12 min (data taken every 15 min). From approximately 5–87 units on time scale, there is an irregular periodic drop in resistivity, interrupted only by a slight diffidence that vanishes quickly, followed by resumed drop. Resistivity of PdD had gone over the hump (near D/Pd = 0.74) at the beginning of the run. This assured the specimen was above the range of average D/Pd = 0.93 for the events featured here and all events of excess power and heat. What makes this drop particularly significant is the fact that temperature of the cell is increasing all the time resistivity is changing. This is shown in Fig. 24 along with the temperature increase of the cell during resistivity drop. These events could be triggered by a sudden increase in current density, but they also happened, most often, spontaneously at constant current density.

Figure 24. Left cell (Pd/Pt) in D_2O exhibiting excess power with the specimen above an average D/Pd = 0.93. The drop in voltage is from a change in resistivity since electromigration current is constant and the temperature of the cell is increasing and electrolysis current density is constant.

5. Discussion

The magnitude of excess heat (Figs. 21 and 22) confirms Fleischmann–Pons heat effect from nuclear origin. The amount of excess heat per cubic centimeter of Pd (150 MJ/cm^3) or per Pd atom (14 000 eV/atom) is too large for a chemical reaction, which produces energy per atom less than 2 eV/atom. The drop in resistivity while temperature increases, is not expected behavior of PdD. Most metals and metal hydrides (or deuterides) show increasing resistivity with temperature [54–56], as in Fig. 25. Nucleation of a new phase, other than beta (β) or gamma (γ), with lower resistance is likely occurring in Figs. 23 and 24. If excess heat is from δ (Pd$_3$VacD$_4$ with D in octahedral sites), then formation of δ' (Pd$_3$VacD$_4$ with D in tetrahedral sites) (Fig. 26) enables extensive pathways of low resistance for
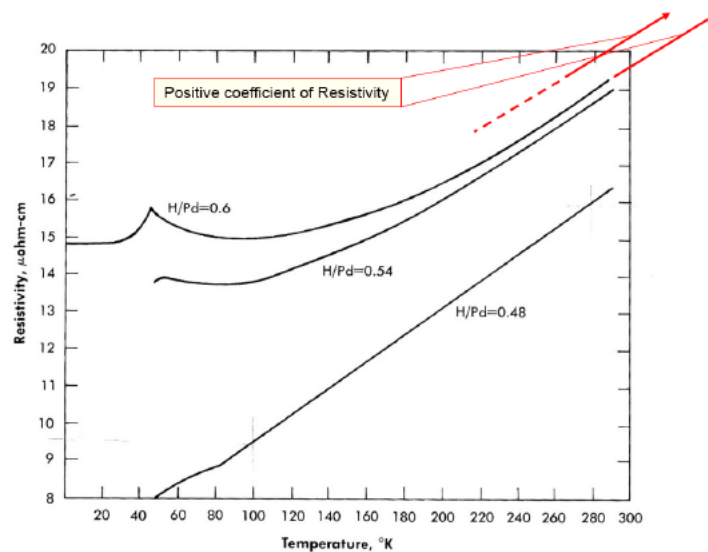
Figure 25. Resistivity versus Temperature for Pd–H samples from low temperature to room temperature and extrapolated to temperatures above room temperature with a positive coefficient of resistivity, from [54,55].

electron transport along tubes, which are vacancy channels free of atoms along edges of unit cells. These extend from one unit cell to the next and intersect at all unit cell corners, as shown in Fig. 27. The solubility of D(H) decreases with increasing temperature in Pd–H [57–59] and decreases in Pd–Ag alloys, as shown by Paolone et al. [60]: they are exothermic [57]. With current density constant, fugacity is constant. Phase change to tetrahedral site occupancy is a change with more order as Isaeva et al. [29] indicate: tetrahedral site occupancy is favored as a more ordered phase. Resistivity, in general, is larger in a disordered state than in an ordered state, as pointed out by Fukai [61]. Therefore, the specimen is unlikely to be further loading itself with D (to lower resistivity), but rather more likely to be undergoing phase change from δ to δ'. As there is insufficient time for δ or δ' to form at room temperature by vacancy diffusion this is not the formation mechanism of SAV ordered phases. Appendices A and B are an alternative of supplying vacancies at small SAV volume fractions for a mixed phase composite microstructure in the bulk (β with small islands of δ or δ'). The δ is estimated below to be 0.03%: thus not many vacancies are required. The co-deposit work that results in SAV at room temperature show: SAV phases form and are stable at room temperature (equilibrium phases, not meta-stable phases). If SAV phases are merely formed at elevated phases and then quenched-in at room temperature then they would be meta-stable and would decompose to an equilibrium form (another that is not an SAV phase) but they do not.

Sites for nucleation of δ' would be less than the total volume fraction f_v of δ-phase in the cathode. This fraction is the active atoms divided by total atoms, determined as follows. The number of Pd atoms in specimens here is $= 3.4 \times 10^{20}$ atoms (size of Pd, Section 3), while nuclear reactions could produces 23 800 000 eV per reaction. The actual energy produced is 14 000 eV/Pd atom or 7000 eV/(D atom pair) over 46 days. Thus $f_v = 7000/23\,800\,000 = 0.0003 = 0.03\%$. The total number of D pairs participating $= 1.0 \times 10^{17}$ pairs out of 3.4×10^{20} atoms. If all of the δ-phase is active in giving heat, then f_v is too small to detect δ-phase from metallurgical microscopy. The δ'-phase is an even smaller fraction, yet it produces a macroscopic effect (measurable lowering of overall resistivity of the bulk specimen). This implies the inherent resistivity of δ' is very low (possibly even zero) since the total resistance of the cathode must obey the law of mixtures, combining resistivity of δ' times its small volume fraction with resistivity of
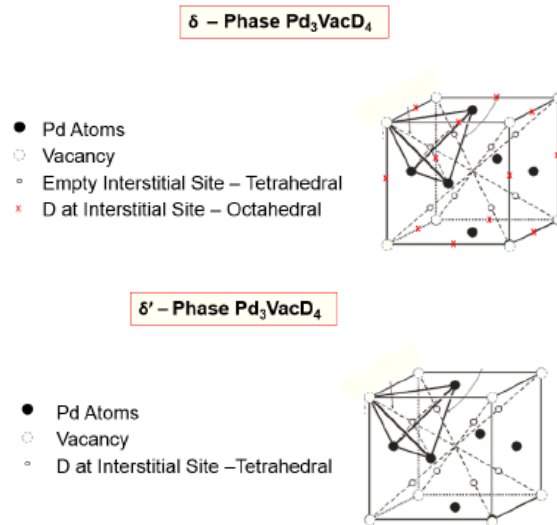
Figure 26. The ordered unit cells of the delta (δ), Pd_3VacD_4 and delta prime (δ'), Pd_3VacD_4-phases. The main difference is that D occupies octahedral sites in δ and tetrahedral sites in δ'. Edges of the unit cell in δ' are straight paths of open tunnels (*or tubes*) because of vacant Pd atoms. In δ, the only atoms in these tubes are D^+ ions.

beta β times its volume fraction (complement fraction). Thus, there is significant variation in resistivity from location to location within the bulk. This is consistent with observed local hot spots for production of tritium observed by Will et al. [62] and Srinivasan et al. [63]. It is also consistent with small and scarce local explosive reactions in the lattice in near-surface region from volcanic-like eruptions observed in optical and scanning electron microscopy of the surface after excess heat [64].
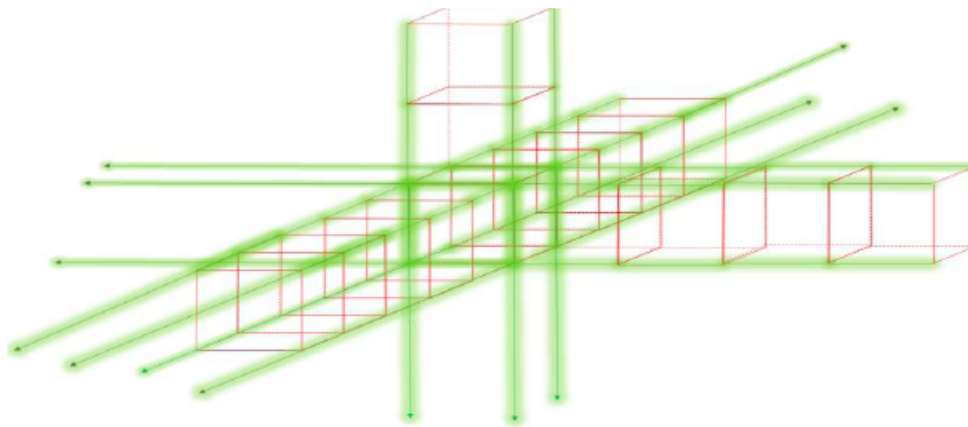
Figure 27. Tubes (*green*) on all edges of unit cells of delta (δ), and delta prime (δ')-phases are a network of intersecting tunnels producing a separate open tube lattice of its own.
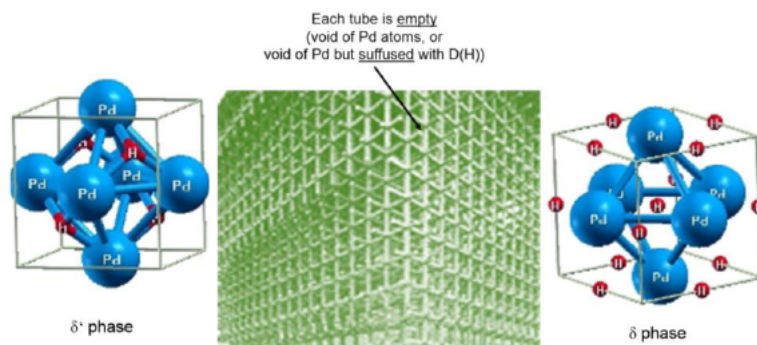
Figure 28. Tubes for each unit cells of either δ or δ'-phases. These phases form a 3-D vacancy tube lattice or network of intersecting tunnels. The tube lattice (*green*) has Pd and isotopic hydrogen in the space between tubes in δ' (left image = Pd$_3$VacD$_4$ - T), or has only Pd atoms (right image = Pd$_3$VacD$_4$ - O) in the space with D$^+$ *inside* the tubes in δ. Unit cell images (*blue and red*) after [29].

The tube lattice (Fig. 28) has Pd atoms nested between tube *intersections*: either Pd with D(H) or only Pd, depending on whether the phase is δ' or δ (with D still inside the tubes). If D is still inside tubes (δ) as an ion, then this is a variant of Storms' model [65]: an electron in between each D$^+$ ion (Fig. 29). Storms' model might be improved by replacing a two-dimensional crack with a one-dimensional tube of diameter equal to about one Pd atom. The tube would maintain alignment and avoid the buckling problem inherent in two-dimensional crack space. Electron shielding, in two-dimensions, needs to be kept aligned to avoid instability (D(H) ion and electron pop sideways). The tube would keep the shielding aligned and avoid elastic buckling instability as in axially loaded beams in compression, Euler Buckling. In addition real metal cracks may be too wide (not sharp) on an atomic scale to align a string of alternating charges of ions as proposed by Storms [65]. The size and geometry of real cracks are shown in Fig. 30
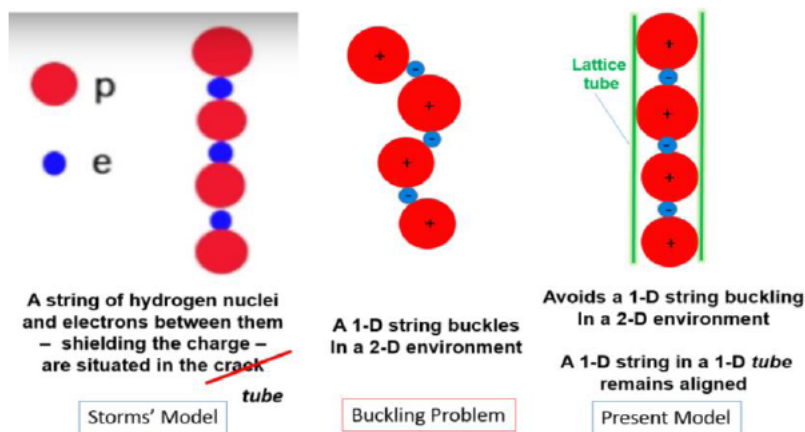
Figure 29. Storms [65] has modeled electron shielding in a two-dimensional crack shown on left and available online: https://www.youtube.com/watch?v=SNodilc6su0. The center shows that a string of alternating electrons and deuterons (*protons*) will buckle when left in a two-dimension crack with a third dimension of width of 1 atom. The present view of SAV in Figs. 26 and 27 corrects the buckling problem since the lattice tube is 1 atom in diameter and maintains alignment when compressed axially.
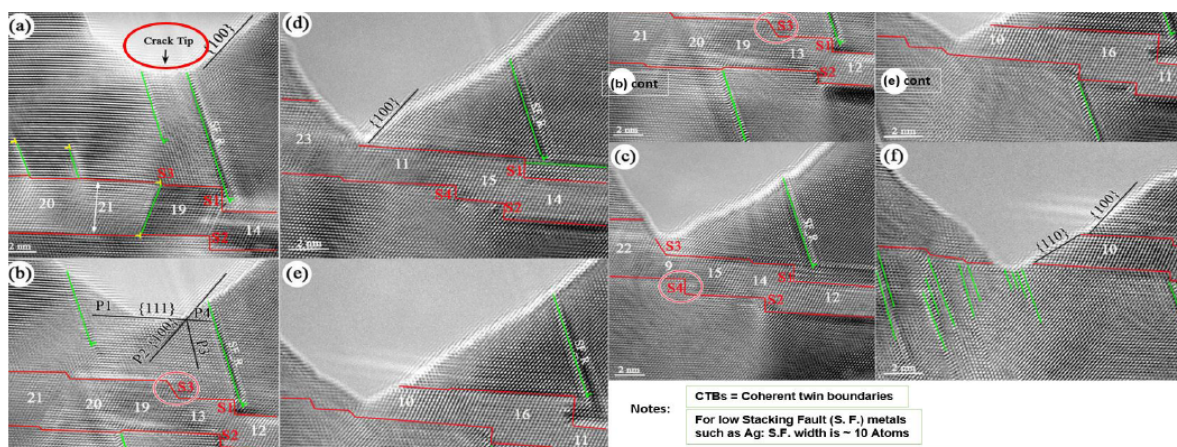
Figure 30. High resolution transmission electron microscopy, HRTEM, images in silver (Ag), a low stacking fault metal: (a)– (c) in situ HRTEM images during the crack propagation in the matric. (d)– (f) in situ HRTEM images during the penetration of the crack across the CTBs. The beam direction is parallel to $\langle 110 \rangle$. The CTBs are outlined in red lines and the corresponding twin thickness is labeled in the unit layers. A stacking faults marked as SF_R is chosen as the reference. The crack surface changes from { 100} to {110} after the crack penetration across the CTBs. P1–P4 in (b) indicate slip planes. Crack is too large to support an aligned string of alternating deuterons and electrons. adapted from [66].

adapted from [66] who used high resolution transmission electron microscopy HRTEM to document images at tips of cracks in silver (Ag), a low stacking fault metal. Pd is a higher staking fault metal (approximately 10 times higher).

This model of a regular lattice of tubes filled with an alternating pattern of deuterons and electrons is very different from previous models of multiple deuterons in a monovacancy such as the work of Nordlander et al. [67]. In addition, the local source of vacancies, from severe plastic deformation (SPD) by intersecting dislocations, and the effects of electromigration for minor relocation effects may present additional issues from those discussed by McLellan and Zang [68] related to the kinetics of vacancy migration. Additionally, these issues are directly related to kinetics (rate of production) rather than thermodynamics (stable phases). The kinetic problems were by passed in the work of Szpak et al. [69] and fellow researchers Letts and Hagelstein [70] who obtained excess heat by purposefully creating vacancies directly with co-deposition at high current density.

6. Summary and Conclusions

(1) The energy produced, over and above input energy, was 150 MJ/cm^3 of Pd (14 000 eV/Pd atom) for 46 days. The average excess power ranged from 4.7$\pm$ 0.15 to 9.6$\pm$ 0.30 % of input power while input power ranged from 2.000 to 3.450 W, confirming the Fleischmann–Pons effect. The energy release was of such magnitude that the source is nuclear. The exact nuclear reaction was not determined in this work.

(2) Two run-away events were triggered by suddenly increasing current density resulting in 100 % excess power (2.4 W output with 1.2 W input) necessitating a temporary cut back in electrolysis current.

(3) The emended palladium–isotopic hydrogen phase diagram is presented: Three new phases, from XRD results from recent literature, are shown on the phase diagram as superabundant vacancies (SAV) phases and are: γ-phase (Pd$_7$VacD$_{6-8}$), δ-phase (Pd$_3$VacD$_4$-octahedral), δ'-phase (Pd$_3$VacD$_4$-tetrahedral). These phases are the lowest free energy phases at their respective compositions.

(4) Resistivity of Pd was used to assay D activity in the Pd lattice (ratio of D/Pd) and employed as an indicator of phase changes. The excess heat supports portions of the cathode being in the ordered δ-phase (Pd$_3$VacD$_4$-

octahedral), while the drop in resistance of the Pd cathode during increasing temperature and excess heat indicates portions of the cathode transformed to the ordered δ'-phase (Pd$_3$VacD$_4$-tetrahedral).

(5) The structure of δ-phase (Pd$_3$VacD$_4$-octahedral) and δ'-phase (Pd$_3$VacD$_4$-tetrahedral) show a network or lattice arrangement of empty tubes (δ') or tubes filled with isotopic hydrogen (δ). These empty tubes provide extensive pathways of ultra-high mobility of hydrogen (δ) or electrons (δ') or both. It is proposed these tubes provide a pre-condition of nuclear activity.

(6) A model of electromigration is presented where these phases were encouraged by electromigration current, causing D$^+$ ions (trapped to vacancies) to pull vacancies along and aid the formation of SAV phases. The model of electromigration indicates considerable enhancement of D$^+$ ions (higher D/Pd) at one end of the specimen raising the likelihood of SAV phases and nuclear activity.

(7) A plastic deformation based model offers a mechanism for vacancy production in the bulk lattice. Vacancies are created by dragging of jogs connected between screw dislocations. Jogs are created by intersecting dislocations. The creation and mobilization of these vacancies raise the likelihood of SAV phases and nuclear activity by mitigating the necessity for bulk diffusion from the surface or grain boundaries. It shows the importance of plastic deformation (by cold work or by a loading/unloading/reloading sequence) in preparing Pd (or Ni) specimens for LENR.

Acknowledgements

Appendix A. Effects of Electromigration on Enhancing the Concentration

Early work on isotopic hydrogen ion migration from an electric field in metal lattices began with Coehn [71], co-workers [72–74] and others [75,76]. It was applied to LENR promptly by several groups [77–84]. Bartolomeo et al. [79] predicted in 1993 about the time SAV phases were being discovered that: It is certainly possible that a further phase transformation takes place at high D:Pd ratios leading to the formation of a γ-phase and that it is the properties of this phase which will explain the nuclear processes induced in Pd and Pd-alloy host lattices. This prediction seems to be born out for δ rather than γ, as in this work. The Preparata-Effect [84] uses a very long thin wire with as high a total voltage drop as possible along the wire (axial voltage drop) but with as low an axial current as possible for electromigration. Here the opposite (low voltage drop with high current) is sought. Low voltage drop minimizes parasitic joule heating (for a given current), and high current causes electromigration, but also contributes to joule heating, which must be balanced against electromigration.

Specimens were supported in cells between heavy gauge Cu wire leads. D$^+$ electromigration was effected by passing current for enhancement of D concentration along the length as in Fig. 31. Fluxes in opposite directions, $J_{D+}^{electricfield}$ and $J_D^{concentration}$, balance at steady state (after transient period). Flux $J_{D+}^{electricfield}$ due to electric field ($E = dV/dx$) is $nq\mu E$, where n is number of charges, q charge assigned to D$^+$ ($\sim$-e), and μ is mobility ($= D/k_BT$). Electrons and protons (deuterons) have different mobilities: for electrons $\mu = 1/nq\rho$, where ρ is resistivity in cm-Ω, but deuteron mobility, from Nernst–Einstein equation, is $\mu = D/k_BT$, where k_B is the Boltzmann constant and D is diffusion coefficient. With Fick's first law, $D(dC/dx) = nq\mu E$, a first order differential equation. If dC/dx is C' and dV/dx is V', and since $C = n$, the equation is $C' = C\,S\,V'$, where S is defined as q/k_BT. The solution is: $C(x) = Be^{SV}$, where B is a constant from boundary condition: $C(x = 0) = C_o$ and $V(x = 0)$ can be defined as V_o. With these and the boundary condition: $C(0) = Be^{SVo}$ with $B = C_oe^{-SVo}$. The solution is: $C(x)/C_o = \exp(q[V(x) - V_o]/k_BT)$, or if Z is defined as (q/e^-), then $C(x)/C_o = \exp(Ze[V(x) - V_o]/k_BT)$. This equation
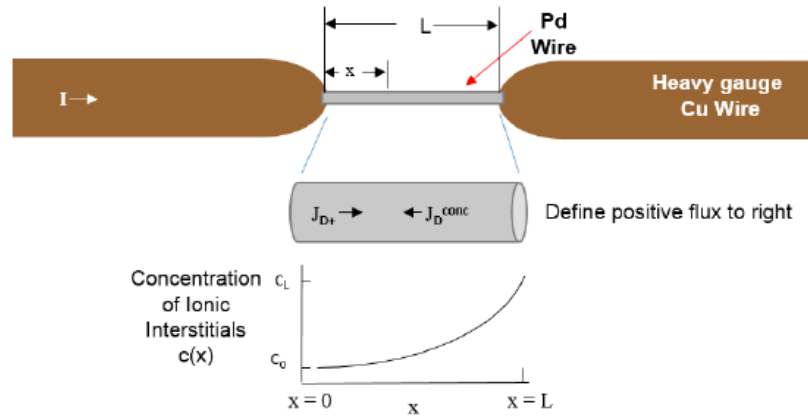
Figure 31. Pd between two Cu leads, the two fluxes that develop and the resulting concentration profile.

was independently published before the discovery of LENR [85], but, as far as the author knows, was first applied to LENR in 1991 [77,78] and shortly thereafter [79–84]. For rod of uniform section A ($= \pi d^2/4$) and resistivity ρ, $E = [V(L) - V(0)]/L$ and $E = I\rho/A$, thus $[V(L) - V(0)] = I\rho L/A$. Then $C_L/C_o = \exp(4Ze I\rho L/\pi d^2 k_B T)$. Evaluating with numbers gives: $C_L/C_o = \exp(0.0003723 IL/d^2)$ for $z = 0.7$ and $C_L/C_o = \exp(0.0005319 IL/d^2)$ for $z = 1$. Table 1 shows electromigration effects are significant, in terms of concentration at one end versus the other end (i.e., C_L/C_o). For values of currents used (typically 3 A, but as high as 10 A), the enhancement is from 506 to 22 200%. If actual enhancement were only 40% it would be significant. It should be pointed out, the parasitic heat added could be significant if specimen size is imprudently selected, but for the conditions here (3 A) it was about 0.1 W.

Table 1. Composition enhancement from one end to the other by electromigration in Pd[a].

Total current, I (A)	Diameter of specimen, d (cm)	Power density by Joule heating , P (W/cm^3)	Total power ($= P \times$ volume of specimen) (W)	Composition ratio (enhancement) C_L/C_o (= C(L)/C(0))	
				$Z = 0.7$	$Z = 1$
1	0.10	0.175	0.0035	1.10	1.14
3	0.10	1.58	0.0314	1.33	1.50
10	0.10	17.5	0.349	2.57	3.86
20	0.10	70	1.40	6.60	14.91
1	0.05	2.80	0.014	1.46	1.72
3	0.05	25.21	0.126	3.10	5.06
10	0.05	280	1.40	44.0	222.0
20	0.05	1121	5.59	1902.0	49 425.0

[a]*Note*: Using $\rho = 10.8 \times 10^{-6} \Omega$-cm, $L = 2.54$ cm, temperature (300 K) and constant diffusion coefficient, electric wind force at zero, steady state is assumed (transient period is proportional to length^2/diffusion coefficient, L^2/D) and no leakage back into electrolyte along the specimen surface (the highest potential). Thus, $C/C_o = \exp(0.0005319 IL/d^2)$, for $Z = 1$. Joule heating (total power = $P\times$ volume of specimen) uses $P = 0.000017508 I^2/d^4$ in W/cm^3.
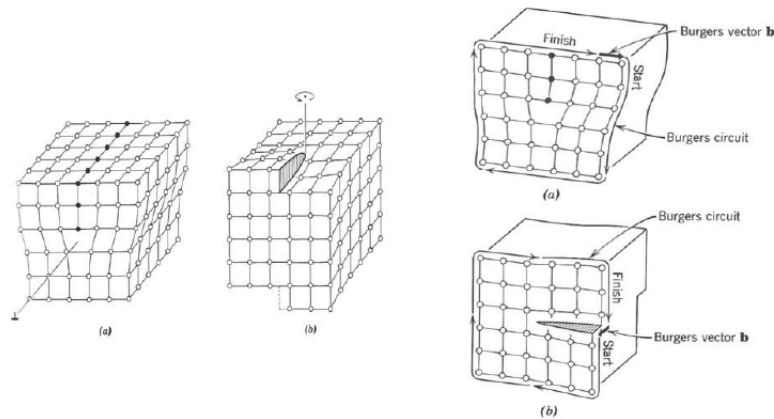
Figure 32. Geometry (*Left*) and Burgers circuits (*Right*) around Edge (a) and Screw (b) Dislocations. After [87].

Appendix B. A Plastic Deformation Mechanism for Creating Apposite Interior Vacancies

A well-known mechanism [86–88] to create vacancies through screw dislocation intersections that generate jogs evidently plays an important role in pre-processing Pd for LENR. Loading and unloading Pd with D four times (three times unloading, seven times through the miscibility gap) encouraged a well-developed dislocation cell structure and its associated excess of vacancies. The Burgers vector for edge dislocations is always perpendicular to the dislocation line and screw dislocations have Burgers vectors parallel to the dislocation line, Fig. 32. Jog-components of dislocations in the slip plane (called kinks) can be either screw or edge (Fig. 33). When dislocations intersect, they always create jogs (Fig. 34). For purposes here, the most important type of intersections are intersections with screw dislocations. Dislocations intersect during heavy cold work. Wen et al. [89] have shown hydrogen enhances homogenous dislocation nucleation, promotes dislocation emission, induces slip planarity, and localizes dislocation activity significantly, leading to locally enhanced vacancy formation from dislocations. In Fig. 34, both screws (<u>AB</u> moving along the slip plane, ABCD) and edge (<u>BC</u> moving left to right on slip plane) components of curved dislocations can create jogs. Unlike kinks, a jog is normal to the main slip plane and resists being dragged by a screw dislocation because it either creates lattice-atom interstitials (moving to the right in Fig. 35 and requiring higher energy), or it creates lattice-atom
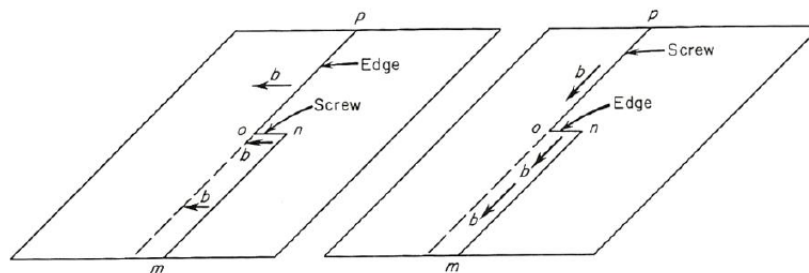
Figure 33. Edge and screw dislocations with Jogs in the slip plane. Jogs in the slip plane are called Kinks. Jogs out of the slip plane are called jogs. Dislocations *mnop* in the slip plane (the plane containing dislocation and burgers vector *b*) with a kink section *on* where its nature changes from edge to screw (*left*) or screw to edge (*right*). Here the kink *on* lies *in* the slip plane, adapted from [88].
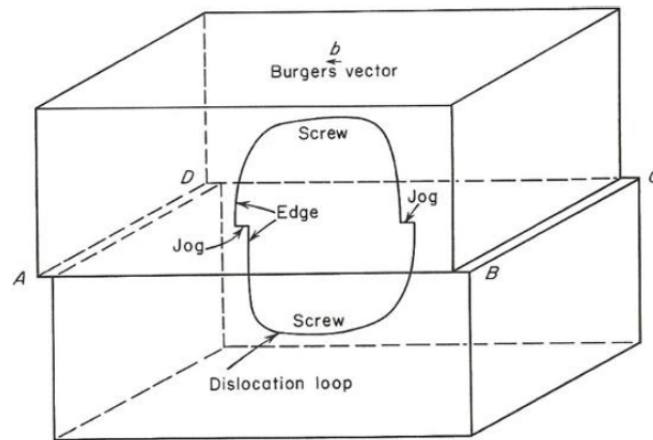
Figure 34. An *edge* dislocation parallel to BC or AD moves from left to right on slip plane ABCD, it cuts through the vertical portion (*edge*) of the dislocation loop creating jogs on the edge portion of the loop. The same would happen if a *screw* dislocation parallel to AB moved from front to back on plane ABCD: it would create the steps at BC and AD and the jogs shown, consistent with its Burgers vector *b*. These jogs are screw in nature (*parallel to b*), but if a dislocation cuts the screw portion of the loop, by moving on a vertical plane, it would create a jog with edge nature, adapted from [88].

vacancies (moving to the left in Fig. 35 and requiring less energy). The red area in Fig. 35 is a row of vacancies created behind the right-to-left moving screw dislocation with an edge jog. Dislocation intersection happens by millions in heavy deformation and is a source of *interior-created* vacancies (as opposed to diffusion *bringing* vacancies from surfaces or from grain boundaries).

In addition to this mechanism for creating vacancies at interior positions in the solid, electromigration, (Appendix A) drags vacancies along with migrating D^+ ions because of binding energy between vacancies and interstitial hydro-
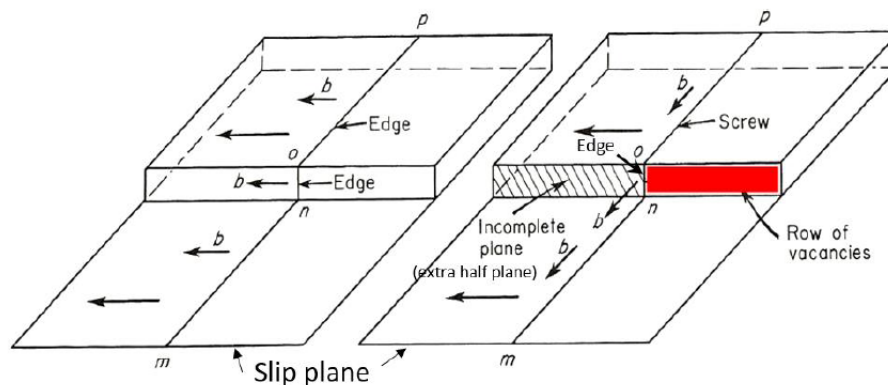
Figure 35. Dislocation *mnop* where its nature is all edge (*left*) or mostly screw (*right*) in a slip plane with a section *on* (jog). The jog *on* is **normal** to the main slip plane (*not a kink*) and is edge in both cases. When the jog on the right, connected to screw components, moves to the left, it must create a row of vacancies behind it (*red section*) because its nature is edge and its Burgers vector b is perpendicular to motion. This is not true of the edge dislocation and its jog on the left because of differently oriented *b*, adapted from [88].

gen. The volume of the nuclear active environment (NAE) is a small percent of bulk volume (Section 5), so the amount needed, by these two mechanisms, to produce a NAE is relatively small.

Dislocations intersect and tangle into dislocation cells and cell size d is controlled by dislocation density $\rho (d = K\rho^{-1/2})$ which is also related to shear flow stress $\tau (\tau = 0.57\, Gb\, \rho^{1/2})$ and thus hardness, as shown theoretically by Holt [47] for all metals with high enough stacking fault energy, and then first shown experimentally for Cu [48] and subsequently most other metals [49]. Here G is shear modulus and b is Burgers vector. Dislocation cell formation occurs in unalloyed Pd and PdH as found experimentally by Deutges et al. [50]. For PdH cells form except, with hydrogen uptake there is higher dislocation density and smaller cell size ($d = K\rho^{-1/2}$ and $\tau = 0.57\ Gb\rho^{1/2}$), consistent with higher hardness results (higher τ) shown above (Fig. 16). There are more vacancies from the jog mechanism when H(D) is present. High vacancy content associated with high hydrogen content found in density functional perturbation theory (DFT) supports the result of this dislocation-based vacancy producing mechanism.

Millions of such intersecting events with the associated row of vacancies stretching across the dislocation cell occur during dislocation cell formation in metals, providing a supply of vacancies large enough to support nucleation and growth of SAV phase islands within the β-phase since the volume fraction of δ is only 0.03%. These rows of vacancies are then dispersed by electromigration and very local diffusion to the eight corner positions of SAV units cells. This mechanism supplants thermal generation of vacancies and diffusion from the surface or grain boundaries which is too slow at room temperature to provide the number of vacancies needed for SAV phases. The final microstructure consists of a two-phase microstructure of predominately β with small islands of δ. Dislocation cells form under plastic deformation with dislocation density around 10^{10}–10^{12} cm per cubic centimeter [47–50, 89]. Plastic deformation is inferred to be essential for creating the nuclear active environment.

An estimate of the adequacy of this mechanism in providing vacancies can be made as follows. In a single dislocation cell of typical size of 1 μm, there will be 3636 vacancies created in the row of vacancies as jogged dislocation ABCD traverses the dislocation cell shown in Fig. 36. This is simply the ratio of the length of the row (10^{-6} m, cell size in PdH, see Fig. 5 of Ref. [50]) divided by the size of the vacancy in Pd (2.75×10^{-10} m). The number of FCC
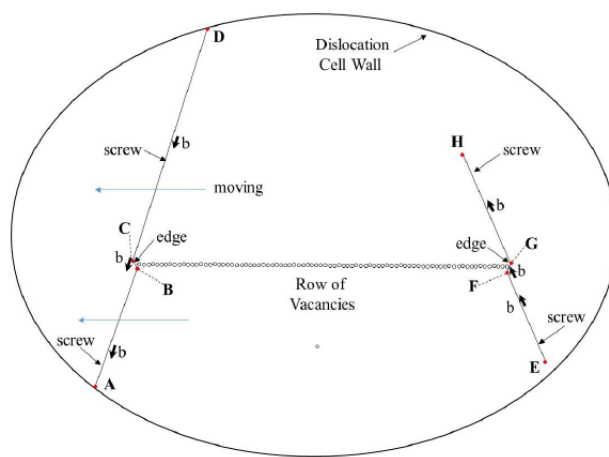
Figure 36. Dislocation ABCD, one of many jogged screw dislocations moving left across the dislocation cell dragging the edge jog component BC and creating a string of vacancies in its wake back to dislocation EFGH. The jogs BC and FG were created by the intersection of original screw dislocations AD with EH. Intersecting dislocation (EFGH) has its Burgers vector b parallel to the edge component BC, and dislocation ABCD has its Burgers vector parallel to the edge component FG, as shown. Dislocation EH was perpendicular to the glide plane of dislocation AD, assumed for the sake of illustration, to be the plane of the paper.

unit cells within this dislocation cell is 8.9×10^9 (ratio of volume of the dislocation cell, $4/3 \, \pi d^3/8 = 0.52 \times 10^{-18}$ m^3, divided by the volume of the Pd FCC unit cell $= 5.89 \times 10^{-29}$ m^3, the cube of the lattice parameter): see note [90]. The lattice parameter of Pd is 3.89×10^{-10} m. Since there is one vacancy per SAV unit cell (δ-phase, Pd$_3$VacD$_4$), the number of vacancies required is the same as the number of new SAV unit cells created by this mechanism. The number of new SAV unit cells in the dislocation cell is 2.7×10^6, which is the nuclear active volume fraction of δ, ($f_v(\delta) = 0.0003$, see Section 5) times the number of FCC unit cells in the dislocation cell (8.9×10^9). Therefore the number of intersections of dislocations in the dislocation cell needed to supply the vacancies is 743. This is the ratio of vacancies need (2.7×10^6) divided by the number of vacancies per intersection (3636). For dislocation density of about 10^{11}cm per cubic centimeter [47–50,89], it would become 0.1 cm per the dislocation cell volume when proportioning the volume from a cubic cm to the volume of the dislocation cell ($d = 10^{-6}$ m, volume $= 0.52 \times 10^{-18}$ m^3). This number is expected to be about 10–100 times larger under sever plastic deformation. Using 0.1 cm, this can be thought of as 10^3 dislocations whose sum of their lengths is 0.10 cm. inside the disloction cell. If another dislocation passed through the dislocation cell, it would make 10^3 intersections with these dislocations. Since this number is greater than (or the same order as) 743, the dislocation jog mechanism is able to supply the necessary number of vacancies to form the required volume percent of δ-phase that is nuclear active. This number could be higher by a factor of 10–100 if 10–100 dislocations intersect the 10^3 dislocations of length 0.1 cm instead of just the one considered here. Therefore, diffusion of vacancies from the surface or from grain boundaries is not required to form nuclear active SAV phase (δ) at room temperature. It may not be a coincidence that the geometric row of vacancies created in this mechanism is a convenient precurser of the vacancy tubes referred to in Fig. 28.

Appendix C. X-ray Diffraction Evidence for SAV Structures

The XRD evidence for SAV relies on the ability to distinguish crystal (Bravais) lattices and lattice parameters. Simple cubic (SC) and face centered cubic (FCC) are two Bravais lattices involved in SAV structures and can be distinguished because of the structure factor [91] for each unit cell. The resultant wave scattered by all atoms of the unit cell is called the *structure factor* $\boldsymbol{F}_{\mathbf{hkl}}$ for the hkl reflection (diffraction), given by:

$$F_{\mathbf{hkl}} = \sum\nolimits_{n=1}^{N} f_n \mathrm{e}^{2\pi i (h u_n + k v_n + l w_n)},$$

where f_n are the atomic scattering factors (ratio of the amplitude of the wave scattered by atoms to the amplitude of the wave scattered by the electron) of each atom n in the unit cell, hkl are the Miller Indices of the plane of diffraction, uvw are the fractional coordinates of atom positions within the unit cell, and N is the total number of atoms in the unit cell. $\boldsymbol{F}_{\mathbf{hkl}}$ is a complex number with both amplitude and phase, but its absolute value $|\boldsymbol{F}_{\mathbf{hkl}}|$ is a ratio of amplitudes:

$$|\boldsymbol{F}_{\mathbf{hkl}}| = \frac{\text{amplitude of wave scattered by all atoms of the unit cell}}{\text{amplitude of the wave scattered by one electron}}.$$

In addition to Bragg's law for determining when reflections at a given angle, θ, occur, the structure factor changes the intensity of a pattern of hkl reflections. Some reflections have zero intensity ($|\boldsymbol{F}_{\mathbf{hkl}}| = 0$) when adding the scattering for each atom in the unit cell. The results of $|\boldsymbol{F}_{\mathbf{hkl}}|$ for these zero intensity calculations (missing reflections) are summarized in Table 2 for selected Bravais lattices, whereas only those reflections that are *present* are listed in Table 3. The presence of the *red* (Superlattice lines) indices verses only the *black* (fundamental lines) indices in Table 3 determines if the Bravais lattice is SC or FCC. When the unit cell changes from FCC to SC Superlattice lines (red indices) appear in the XRD patterns. This was first discovered by Sykes and Evans in the gold–copper (Au–Cu) alloy with an ordered structure, AuCu$_3$ [92] and is shown in Fig. 37. XRD evidence in PdD(H) for SC instead of a FCC

Table 2. Present and missing reflections (diffracted) conditions for common Bravais lattices.

Bravais lattices type	Reflections present[a]	Reflections missing[a]
Simple	All	None
Base-centered	h and k unmixed[b]	h and k mixed[b]
Body-centered	$(h + k + l)$ even	$(h + k + l)$ odd
Face-centered[c]	$h, k,$ and l unmixed	$h, k,$ and l mixed
Hexagonal close packed	$(h + 2k) = 3$ integer, l is odd	All other cases

[a]Planes denoted by Miller Indices h, k, l defined as reciprocals of the fractional intercepts which the plane makes with the crystallographic axes.

[b]Applies to a cell with the base (face with atom at center) as the C face (plane defined by axes a and b), if base is B face (defined by a and c axes), then h and l are unmixed when reflection is present, and if base is the A face (defined by b and c), then k and l are unmixed when reflection is present.

[c]Also includes all NaCl-type structures except when $f_{\text{Na−type atom}}$ happens to equal $f_{\text{Cl−type atom}}$.

proves the unit cell is either δ-phase (Pd$_3$VacD$_4$- octahedral) or δ'-phase (Pd$_3$VacD$_4$- tetrahedral), rather than beta β-phase (PdD). But δ cannot be distinguished from δ' by XRD alone because the atomic scattering for D(H), f_D, is so small, but neutron diffraction can distinguish them. For Pd when vacancies replace corner atoms of the unit cell, it takes the same ordered arrangement as Cu$_3$Au. Examining this unit cell and considering corner vacancy as an atom-type, one sees that for every vacancy fully within the unit cell (1/8 of each of eight corner atoms), there are three Pd atoms fully within the unit cell (1/2 of each of the six face atoms). Clearly the vacancy-atoms, by themselves, form a simple cubic unit cell and so the Pd$_3$Vac ordered unit cell is SC. Its structure factor confirms SC with both fundamental and superlattice reflections. Figure 38 shows the XRD pattern for the SAV form of Pd-hydride at 500°C and H pressure of 5 GPa, after holding at 800°C for 3.5 h and another sample at 300°C and H pressure of 5 GPa, after holding at 700°C for 8.5 h from [93]. There has been separation into two phases PdH (A) and a vacancy-ordered phase Pd$_3$VacH$_4$ (B). The latter phase (B) is identified as SC from the superlattice lines. Figure 39 shows the same behavior for NiH processed at 800°C and H$_2$ pressure of 5 Gpa from the work of Fukai et al. [94]. Superlattice reflections indicate the crystal lattice is also simple cubic (ordered phase, Ni$_3$VacH$_4$).
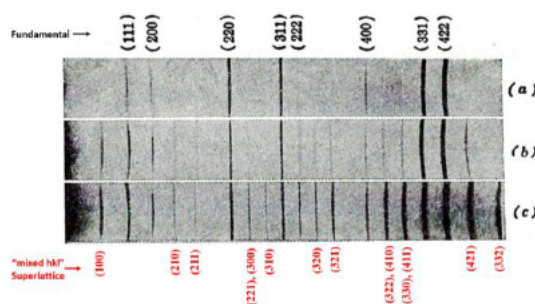
Figure 37. Powder XRD pattern (reflection line intensity recorded on film) of the development of order in an FCC Au–Cu alloy: (a) disordered (fundamental reflections), (b) partially ordered, and (c) highly ordered AuCu$_3$ with Superlattice reflections, adapted from [92].

Table 3. Reflections present for each Bravais lattices.

$(h^2 + k^2 + l^2)$ (order of reflection is increasing θ)[a]	Simple cubic (SC) Reflections present = (All hkl)	Face centered cubic (FCC) (including NaCl-type) Present = ($h, k,$ and l unmixed)
1	*100* [b]	c
2	*110*	–
3	*111*	111[c]
4	*200*	*200*
5	*210*	–
6	*211*	–
8	*220*	*220*
9	*221*	–
9	*300*	-
10	*310*	–
11	*311*	*311*
12	*222*	*222*
13	*320*	–
14	*321*	–
16	*400*	*400*
17	*322*	–
17	*410*	–
18	*330*	–
18	*411*	–
19	*331*	*331*
20	*420*	*420*
21	*421*	–
22	*322*	–
24	*422*	*422*

[a]Order: θ increases as $(h^2 + k^2 + l^2)$ since the combination of Bragg's law with d-spacing is:
$\sin^2 \theta_{hkl} = \frac{\lambda^2}{4a^2}(h^2 + k^2 + l^2)$

[b]The numbers highlighted in red color hkl planes indicate the presence of reflections for SC structure called *Superlattice* lines.

[c] Missing reflection for FCC ($\boldsymbol{F_{hkl}} = 0$), and the bold roman numbers hkl planes indicate FCC reflections present called *Fundamental* lines.

Appendix D. Discussion of the Construction of the Pd–D Phase Diagram (Fig. 8)

Phase diagrams dealing with heterogeneous equilibrium (equilibrium involving more than one phase, as opposed to homogeneous equilibrium, involving equilibrium within a single phase, like gas equilibrium) result from having complete equilibrium for the system: there is mechanical (uniform pressure), thermal (uniform temperature) and chemical equilibrium (same chemical potential of each component in all phases, the number of which is P). For heterogeneous system the chemical equilibrium condition demands that the chemical potential of each substance (each component) be identical in every phase which leads to the phase rule: $F = C - P + 2$, where F is the degrees of freedom, defined as the number of variables–temperature, pressure and composition–changes in which can be designated independently without changing the number of phases in equilibrium. Thus F is the number of intensive properties necessary to fix the state of the system. Any homogeneous portion of the system is defined as a phase. Thus different homogeneous portions at the same temperature, pressure and composition are indeed the same phase. Here the components of the system are the individual elements Pd and D. The number of components is C. In this binary system ($C = 2$) there are three primary variables: temperature, pressure and composition. The phase diagram constructed here at constant
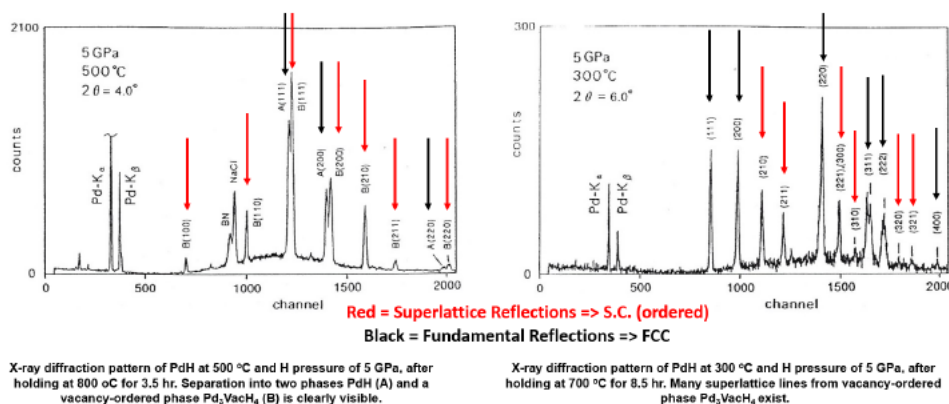
Figure 38. XRD pattern of the ordered unit cells of delta (δ), Pd_3VacD_4) and delta prime (δ'), Pd_3VacD_4) phases. The main difference is that D occupies octahedral sites in δ and tetrahedral sites in δ'. Edges of the unit cell in δ' are straight paths of open tunnels or open tubes because of vacant Pd atoms. In δ, the only atoms in tubes are D^+ ions. Superlattice reflections show the crystal lattice is SC, adapted after [93].

pressure involves only two variables, temperature and composition (thus $F = C - P + 1$). Although the complete depiction of a system involving three variables requires three dimensions, it is common practice to focus on the variables of composition and temperature which are drawn in two dimensions. Thus the equilibrium phase diagram becomes a map of the regions of thermodynamically stable phases wherein the dimensions of the map are composition and temperature. It shows the regions where the combination of temperature and composition result in phases with the lowest free energy (thermodynamic equilibrium) and are placed on the diagram for all the combinations of composition and temperature for which this is the case. The phase rule for a binary diagram ($C = 2$) specifies a one-phase region has two degrees of freedom (temperature and composition): one phase occupies an *area* on the equilibrium phase diagram, a phase field. For a two-phase equilibrium condition, there is one degree of freedom (if the temperature is fixed, then the compositions of both phases are fixed since they are in equilibrium. Two-phase equilibrium is shown on the diagram by two lines (straight or curved). These two curves in temperature-composition space representing the set of points where the two phases are in equilibrium with each other and have only one degree of freedom (either temperature or composition, but not both). And finally three-phase equilibrium can only occur at a point (phase rule
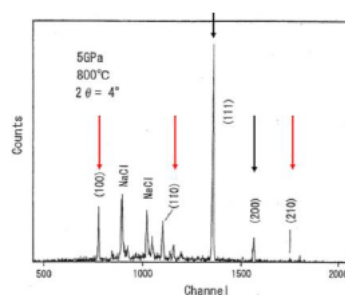
Figure 39. XRD pattern of counts (*intensity*) vs. channel (θ) of Ni_3VacH_4 at 800°C and H_2 pressure of 5 Gpa. Superlattice reflections show the crystal lattice is SC. Sample prepared via high force anvil with NaCl encapsulation to retain hydrogen. Red arrows are reflections from mixed indices (superlattice) while black arrows are from fundamental reflections, adapted after [94].

indicates zero degrees of freedom) called an invariant point. The phase sequence rule follows from these definitions and the phase rule: a single phase region must be followed by two-phase region and be subsequently followed by another single phase region, etc. when traversing the diagram along an isotherm [37].

The phase diagram in Fig. 8 can thus be constructed once the composition of a true equilibrium phase is known: that phase is placed on the map consistent with the temperature and its unique composition. There is allowance for a range of compositions over which the phase is identified as the same phase with homogeneous structure. In this case a homogeneous structure results from having the same crystal Bravais lattice. Bravais lattice is most uniquely identified from XRD patterns (satisfying Bragg's law) of the unit cell that is repeated through a region of space and therefore occupying a volume percent of the whole bulk. Phase diagrams thus also indicate the relative amount of a phase present in the bulk by the lever rule for fields of two phases. Phases occupy a volume percent of the bulk. The admission of the three new phases on the diagram is complete once their nominal (mid-range) composition has been determined from X-ray data. However, it only remains to complete an estimation of the deviation from nominal (stoichiometric) composition while still being regarded as the same phase. Future research will certainly improve on the estimates reported here as more experimental data is accrued regarding the exact positions of the lines on the phase diagram, nonetheless the qualitative layout here is firmly based in thermodynamics, phase diagram construction principles, DFT computations for free energy, and XRD for compositions, and resistivity data for crossing a phase boundary.

Starting with the previously published version of the Pd–D diagram and the newly identified phases from XRD, one proceeds as follows. These phases from the literature (the main section of the paper) γ, δ and δ' must be added to the equilibrium phase diagram according to their compositions if they are true equilibrium phases. Traversing from low to high D/Pd ratio (composition) along an isotherm, there must be a two phase equilibrium field after the β-phase (it must be $[\beta + \gamma]$), followed by a single phase field γ, followed by another two phase equilibrium field (it must be $[\gamma + \delta]$), followed by another single phase field δ, followed by another two phase equilibrium field (it must be $[\delta + \varepsilon]$). The naming of the phases follows phase diagram tradition of the order of Greek alphabet, left to right across the diagram. It was shown from the literature using DFT analysis that these phases are true equilibrium phases so they must be placed on the temperature–composition diagram according to the compositions from XRD data. These data show γ to have compositions of D/Pd ratio 0.85–1.14, based on stoichiometry of $Pd_7Vac_1D_{6-8}$, with nominal stoichiometry D/Pd = 1.0. The range of $D = 6$ to 8 depends on whether the central octahedral site is unfilled in both parts of the dual 4-atom unit cell (consisting of eight Pd atoms) giving a value of D_6, filled in one of the two parts D_7, or filled in both halves of the 8-atom unit cell D_8. The two phase sequence rule is derived from the phase rule; and it is used to verify the width of the $(\beta + \gamma)$-phase field, since β is in equilibrium with γ along the curves, one at 0.76 and the other at 0.85, the beginning of pure γ. The width is simultaneously determined from the data of Araki et al. [42] (where a two-phase field must exist since temperature is constant) and from the phase rule, as shown in Fig. 6. Here composition is the free variable in the phase rule: this results in the same range 0.76–0.85.

Next there must be a single-phase field γ with composition range discussed above (0.85–1.14) followed by the two-phase field $(\gamma + \delta)$. The left-hand side of this field $(\gamma + \delta)$ shares the previous border of D/Pd = 1.14 and extends to D/Pd ratio = x, where x is unsupported by experimental data at this time, but is *assumed* to be 1.24 based on the assumption that both two-phase fields on either sides of γ are symmetrical. This is quantitatively an assumption, but is not an assumption, qualitatively: the exact position of the boundary between $(\gamma + \delta)$ and δ is estimated, but its existence is recognized. The mid-range (exact stoichiometric) value of D/Pd of δ is 1.33 (from Pd_3VacD_4), but this structure exists with some deviation from perfection as to the number of D's filling the octahedral sites. It is not expected to be as wide as γ since γ is an 8-atom unit cell and δ is a 4-atom unit cell. The upper bound of δ shares the same deviation from pure stoichiometry as the lower side. The difference between δ and δ' is that δ has D in octahedral sites and δ' has D in tetrahedral sites. There are eight tetrahedral sites and only four octahedral sites per unit cell. The composition of δ' thus extends to D/Pd = 2.66. The boundary between δ' and δ is determined from the temperature measured during excess heat events: the resistivity of δ dropped. Since D occupies the tetrahedral sites in δ', the edges of the

units cells are completely open for electron transport (low or zero resistivity). From the two-phase sequence rule, there is a two-phase region separating δ and δ' on the left along horizontal temperature traverses (isotherms), similar to the phase diagram of Au–Cu [92,95,96]: the exact width of this two-phase field is not determined here. The ε-phase is anticipated by research data [43,97–99].

Pressure isotherms confirm phase diagram boundaries in three dimensions with the variable pressure along the third dimension. The present work does not explore the variable pressure and its effects on the diagram. Research, such as that of Hagelstein [100–102], forms a more complete picture, with O-site and T-site partition functions as harmonic oscillator partition functions.

References

[1] Ian M. Robertson, P. Sofronis, A. Nagao, M.L. Martin, S. Wang, D.W. Gross and K.E. Nygren, Hydrogen embrittlement understood–2014 Edward DeMille Campbell Memorial Lecture, *ASM International, Metallurgical and Materials Transactions* B, 28 March 2015, DOI: 10.1007/s11663-015-0325-y.

[2] A.K. Eriksson, A. Liebig, Ś. Olafsson and B. Hjorvarsson, Resistivity changes in Cr/V(0 0 1) superlattices during hydrogen absorption, *J. Alloys Compd.* **446–447** (2007) 526–529.

[3] M. Khalid and P. Esquinazi, Hydrogen-induced ferromagnetism in ZnO single crystals investigated by magnetotransport, *Phys. Rev.* B **85** (2012) 134424.

[4] D. E. Azofeifa, N. Clark, W. E. Vargas, H. Solís, G. K. Pálsson and B. Hjörvarsson, Temperature- and hydrogen-induced changes in the optical properties of Pd capped V thin films, *Physica Scripta* **86** (6) (2012) 065702.

[5] S. Kala and B. R. Mehta, Hydrogen-induced electrical and optical switching in Pd capped Pr nanoparticle layers, *Bull. Mater. Sci.* (Indian Academy of Sciences) **31** (3) (2008) 225–231.

[6] H. Noh, Ted B. Flanagan, B. Cerundolo and A. Craft, H-Induced atom mobility in palladium–rhodium alloys, *Scripta Met. et Mat.* **25** (1991) 225–230.

[7] H. Noh, Ted B. Flanagan and M.H. Ransick, An Illustration of phase diagram determination using H-induced lattice mobility, *Scripta Met. et Mat.* **26** (1992) 353–358.

[8] K. Baba, Y. Niki, Y. Sakamoto, A. P. Craft and Ted B. Flanagan, The transition of the hydrogen-induced LI_2 ordered structure of Pd_3Mn to the Ag_3Mg structure, *J. Mats. Sci. Letters* **7** (11) (1988) 1160–1162.

[9] R. Balasubramaniam, Mechanism of hydrogen induced ordering in Pd_3Mn, *Scripta Met. et Mat.* **30** (7) (1994) 875–880.

[10] Scott Richmond, Joseph Anderson and Jeff Abes, Evidence for hydrogen induced vacancies in Plutonium metal, Plutonium Futures–The Science Keystone, CO, September 19–23, 2010, p. 206.

[11] M. Wen, L. Zhang, B. An, S. Fukuyama and K. Yokogawa, Hydrogen-enhanced dislocation activity and vacancy formation during nanoindentation of nickel, *Phys. Rev.* B **80** (2009) 094113.

[12] Y. Fukai and N. Okuma, Evidence of copious vacancy formation in Ni and Pd under a high hydrogen pressure, *Jpn. J. Appl. Phys.* **32** (1993) 1256.

[13] W. A. Oates and H. Wenzl, On the copious formation of vacancies in metals, *Scripta Met. et Mat.* **30** (7) (1994) 851–854.

[14] W. A. Oates and H. Wenzl, On the formation and ordering of superabundant vacancies in palladium due to hydrogen absorption, *Scripta Met. et Mat.* **33** (2) (1995) 185–193.

[15] Y. Fukai, *The Metal–Hydrogen System: Basic Bulk Properties*, 2nd Edn., Springer, Berlin, 2005, p. 216.

[16] Y. Fukai, Superabundant vacancies formed in metal–hydrogen alloys, *Physica Scripta* 2003 No. T103 (2002) 11.

[17] V.F. Degtyareva, Electronic origin of superabundant vacancies in Pd hydride under high hydrogen pressures, Presented on the Conference on Hydrogen Materials Science (ICHMS), Yalta, Ukraine, 25–31 August (2009): http://arxiv.org/pdf/1001.1525.pdf , accessed 25 November 2018.

[18] D. Tanguy and M. Mareschal, Superabundant vacancies in a metal–hydrogen system: Monte Carlo simulations, *Phys. Rev.* B **72** (17) (2005) 174116.

[19] Y. Fukai, Hydrogen-induced superabundant vacancies in metals: implication for electrodeposition, A. Ochsner, G. E. Murch and J. M. O\Q. Delgado (Eds.), *Defect and Diffusion Form* **312–315** (2011) 1106–1115.

[20] D. S. dos Santos, S. Miraglia and D. Fruchart, A high pressure investigation of Pd and the Pd–H system, *J. Alloys Compd.*

291 (1999) L1– L5.

[21] Y. Fukai and N. Okuma, Formation of superabundant vacancies in Pd hydride under high hydrogen pressures, *Phys. Rev. Lett.* **73** (12) (1994) 1640–1643.

[22] Y. Fukada, T. Hioki and T. Motohiro, Multiple phase separation of super-abundant-vacancies in Pd hydrides by all solid-state electrolysis in moderate temperatures around 300 C, *J. Alloys Compd.* **688** (2016) 404–412.

[23] M.P. Pitt and E. MacA. Gray, tetrahedral occupancy in the Pd–D system observed by *in situ* neutron powder diffraction, *Europhys. Lett.* **64** (3) (2003) 344–350.

[24] G.A. Ferguson Jr., A.I. Schindler, T. Tanaka and T. Morita, Neutron diffraction study of temperature-dependent properties of palladium containing absorbed hydrogen, *Phys. Rev*. **137** (2A) (1965) 483.

[25] N. Eliaz, D. Eliezer, D.L. Olson, Hydrogen-assisted processing of materials, *Mat. Sci. Engr*. A **289** (2000) 41.

[26] C. Zhang and Ali Alavi, First-principles study of superabundant vacancy formation in metal hydrides, *J. Am. Chem. Soc*. **127** (2005) 9808–9817.

[27] Y. Fukai, M. Mizutani, S. Yokota, M. Kanazawa, Y. Miura and T. Watanabe, Superabundant vacancy–hydrogen clusters in electrodeposited Ni and Cu, *J. Alloys Compd*. **356–357** (2003) 270.

[28] Y. Fukai, Formation of superabundant vacancies in M–H alloys and some of its consequences: a review, *J. Alloys Compd.* **356–357** (2003) 263–269.

[29] L.E. Isaeva, D.I. Bazhanov, Eyvas Isaev, S.V. Eremeev, S.E. Kulkova and Igor Abrikosov, Dynamic stability of palladium hydride: an ab initio study, *Int. J. Hydrogen Energy* **36** (1) (2011) 1254–1258.

[30] Y. Fukai and H. Sugimoto, Formation mechanism of defect metal hydrides containing superabundant vacancies, *J. Phys. Condensed Matter* **19** (2007) 436201.

[31] H. Sugimoto and Y. Fukai, Migration mechanism in defect metal hydrides containing superabundant vacancies, *Diffusion-fundamentals.org* **11** (2009) 102, pp. 1–2.

[32] L. Bukonte, T. Ahlgren and K. Heinola, Thermodynamics of impurity-enhanced vacancy formation in metals, *J. Appl. Phys.* **121** (2017) 045102-1 to -11. https://doi.org/10.1063/1.4974530.

[33] Y. Fukai and H. Sugimoto, The defect structure with superabundant vacancies to be formed from FCC binary metal hydrides: Experiments and simulations, *J. Alloys Compd.* **446,447** (2007) 474–478.

[34] R. Nazarov, T. Hickel and J. Neugebauer, Ab Initio study of H-vacancy interactions in FCC metals: implications for the formation of superabundant vacancies, *Phys. Rev.* B **89** (2014) 144108.

[35] Y. Fukai, Y. Kurokawa and H. Hiraoka, Superabundant vacancy formation and itsconsequences in metal hydrogen alloys, *J. Jpn. Inst. Met.* **61** (1997) 663–670 (in Japanese).

[36] Y. Fukai, *The Metal–Hydrogen System: Basic Bulk Properties*, 2nd Edn., Springer, Berlin, 2005, p. 10.

[37] H. Okamoto and T. Massalski, Improbable phase diagrams, *J. Phase Equilibria* **12** (2) (1991) 148–168.

[38] J.F. Shackelford, *Introduction to Material Science for Engineers*, 7th Edn., Pearson, Upper Saddle River, NJ, 2009, pp. 272,273.

[39] Tom Callahan and Fiona O'Connell, Studies in EG459**:** special topics in materials engineering–steel metallurgy, Loyola University, Maryland, Fall, 2011.

[40] *Metals Handbook*, Vol. 9, *Metallography and Microstructures*, 9th Edn., American Society for Metals, Metals Parks, OH, 1985, p. 245.

[41] M.R. Staker, The uranium–vanadium equilibrium phase diagram, *J. Alloys Compd.* **266** (1998) 167–179.

[42] H. Araki, M. Nakamura, S. Harada, T. Obata, N. Mikhin, V. Syvokon and M. Kubota, Phase diagram of hydrogen palladium, *J. Low Temperature Phys.* 134 (5/6) (2004) 1145–1151.

[43] Paolo Tripodi, Daniele Di Gioacchino and Jenny Darja Vinko, Magnetic and transport properties of PdH: intriguing super-conductive observations, *Brazilian J. Phys.* **34** (3B) (2004) 1177.

[44] M. Fleischmann and M. Miles. The instrument function of isoperibolic calorimeters: excess enthalpy generation due to the parasitic reduction of oxygen, *10th Int. Conf. on Cold Fusion*, Cambridge, MA, 2003.

[45] T. Sugeno and M. Kowaka, *Mem. Inst. Scientia. Ind. Rese*., Osaka University **11** (1954) 119.

[46] F.A. Lewis, *The Palladium Hydrogen System*, Academic Press, London, 1967, p. 45.

[47] D.L. Holt, Dislocation cell formation in metals, *J. Appl. Phys.* **4l** (1970) 3197.

[48] M.R. Staker and D L. Holt, The dislocation cell size and dislocation density in copper deformed at temperatures between 25

and 700°C, *Acta Met.* **20** (1972) 569.

[49] D. Kuhlmann-Wilsdorf, Theory of plastic deformation: properties of low energy dislocation structures, *Mat. Sci. Engr.* A **113** (1989) 1–41.

[50] Martin Deutges, Hans Peter Barth, Yuzeng Chen, Christine Borchers and Reiner Kirchheim, Hydrogen diffusivities as a measure of relative dislocation densities in palladium and increase of the density by plastic deformation in the presence of dissolved hydrogen, *Acta Mat.* **82** (2015) 266–274.

[51] J.P. Burger, D.S. MacLachlan, R. Mailfert and B. Souffaché, Electrical resistivity of PdH$_x$: 1 - residual resistivity, *Solid State Commun.* **17** (3) (1975) 277–280.

[52] Michael C.H. McKubre, Romeu C. Rocha-Filho, Stuart Smedley, Francis Tanzella, Jason Chao, Bindi Chexal, Tom Passell and Joseph Santucci, Calorimetry and electrochemistry in the D/Pd system, The first annual conf. on cold fusion, Univ. of Utah Research Park, Salt Lake City, Utah: National Cold Fusion Institute (1990), pp. 20–31.

[53] D. Cravens, Factors affecting the success rate of heat generation in cold fusion cells, *Proc. Fourth Int. Conf. on Cold Fusion*, Vol. 2, Calorimetry and Materials Papers, Held Lahaina, Maui, HI, 6–9 December 1993, prepared by Electric Power Research Institute, Pala Alto, CA, TR-104188-V2 (1994), p. 18-1.

[54] A.I. Schindler, R.J. Smith and E.W. Kammer, Low-temperature dependence of the electrical resistivity and thermoelectric power of palladium and palladium–nickel alloys containing absorbed hydrogen, *Proc. Int. Congress of Refrigeration*, Copenhagen, August 19–26, 1959, 10th Congress, Vol. 1, p. 74, Pergamon Press, New York, 1960.

[55] P. Tripodi, M.C.H. McKubre, F.L. Tanzella, P.A. Honnor, D. Di Giacchino, F. Celani and V. Violante, Temperature coefficient of resistivity at compositions approaching PdH, *Phys. Lett.* A **276** (2000) 122–126.

[56] S.L. Ames and A.D. McQuillan, The resistivity–temperature–concentration relationship in β-phase titanium–hydrogen alloys, *Acta Met.* **4** (1956) 609.

[57] W. Mueller, J. Blackledge and G. Libowitz (Eds.), *Metal Hydrides*, Academic Press, NY, 1968, pp. 69 and 82.

[58] F.A Lewis, *The Palladium Hydrogen System*, Academic Press, London, 1967, pp. 7, 9, 22 and 119.

[59] R.A. Oriani, The physical and metallurgical aspects of hydrogen in metals, *4th Int. Conf. on Cold Fusion (ICCF-4),* Lahaina, Maui, HI: Electric Power Research Institute, Palo Alto, CA , 1993.

[60] A. Paolone, S. Tosti, A. Santucci, O. Palumboand F. Trequattrini, Hydrogen and deuterium solubility in commercial Pd–Ag alloys for hydrogen purification, *Chem. Engr.* **1** (2017) 14; pp.1-9 doi: 10.3390/chemengineering1020014 MDPI, Basel, Switzerland.

[61] Y. Fukai, The Metal Hydrogen System–Basic Bulk Properties, 2nd Edn., Springer, Berlin, Heidelberg, New York, 2005, p. 43.

[62] F.G. Will, K. Cedzynska, M.C. Yang, J.R. Peterson, H.E. Bergeson, S.C. Barrowes, W.J. West and D.C. Linton, Studies of electrolytic and gas phase loading of Pd with deuterium, in *Conf. Proc. of Italian Physical Society*, Vol. 33 for 'The Science of cold fusion – Proc. of Second Annual Conf. on cold fusion', T. Bressani, E. Del Giudice and G. Preparata (Eds.), Como, Italy, 29 June –4 July 1991, held at A. Volta Center for Sci. Culture, Villa Olmo, 1991, pp. 373–383.

[63] M. Srinivasan, A. Shyam, T.C. Kaushik, R.K. Rout, L.V. Kulkarni, M.S. Krishnan, S.K. Malhotra, V.G. Nagvenkar and P.K. Iyengar, Observation of tritium in gas/plasma loaded titanium samples, *AIP Conf. Proc. 228–Anomalous Nuclear Effects in Deuterium/Solid System*, 1990. Brigham Young Univ., Provo, UT: American Institute of Physics, New York, p. 514–534.

[64] David J. Nagel, Characteristics and energetics of craters in LENR experimental materials, *J. Condensed Matter Nucl. Sci.* **10** (2013) 1–1.

[65] Edmund Storms, An Explanation of low energy nuclear reactions (cold fusion),
https://www.youtube.com/watch?v=SNodilc6su0, accessed May 15, 2018.

[66] L. Liu, J. Wang, S.K. Gong and S.X. Mao, Atomistic observation of a crack tip approaching coherent twin boundaries, *Scientific Reports,* Vol. 4, Article number: 4397 (2014) doi:10.1038/srep04397.

[67] P. Nordlander, J.K. Norskov, F Besenbacher and S.M. Myers, Multiple deuterium occupancy of vacancies in Pd and related metals, *Phys. Rev.* B **40** (1989) 1990–1992.

[68] R. B. McLellan and D. Zang, Kinetics of vacancy migration in hydrogenated palladium, *Scripta Mat.* **36** (1997) 1207–1210.

[69] S. Szpak, P.A. Mosier-Boss and J.J. Smith, On the behavior of Pd deposited in the presence of evolving deuterium, *J. Electronalytical Chem.* **302** (1991) 255–260.

[70] D. Letts and P.L. Hagelstein, Modified Szpak protocol for excess heat, *J. Condensed Matter Nucl. Sci.* **6** (2012) 44–54.

[71] A. Coehn, Detection (proof of the existence) of protons in metals, *J. Electrochem. (Z. Electrochem).* **35** (9) (1929) 676–680.
[72] A. Coehn and W. Specht, On the participation of protons in the electrical conduction in metals: I. Proof by potential mea-surements, *Zeitschrift fur Physik (J. Phys.)* **62** (1,2) (1930) 1–31.
[73] A. Coehn and H. Jurgens, On the participation of protons in the electrical conduction in metals: II. Resistance measurements, *Z. Phys.* **71** (3,4) (1931) 179–204.
[74] A. Coehn and K. Sperling, On the participation of protons in the electrical conduction in metals: III. The photographic plate as an indicator, *J. Phys. (Zeitschrift für Physik)* **83** (5,6) (1933) 291–312.
[75] B. Duhm, The diffusion of hydrogen in palladium, *J. Phys. (Zeitschrift für Physik)* **94** (1935) 434 and **95** (1935) 801.
[76] C. Wagner and G. Heller, The rate of migration of protons in the electric field in the α-phase of the palladium–hydrogen system, *J. Phys. Chem. (Z. Physik. Chem.)* **46B** (1) (1940) 242–250.
[77] M.R. Staker, private communication to Martin Fleischman, Stanley Pons, Mel Miles and Michael C.H. McKubre, at A. Volta Center for Sci. Culture, Villa Olmo, Como, Italy (29 June–4 July 1991).
[78] M.R. Staker and J.J. Antal, The use of electrostatic field to control the stoichiometry of palladium deuteride in the cold fusion process, a proposal prepared for DOE (April 1992); and a second proposal, Research on control of the cold fusion process and exploration of its nuclear origins, prepared for Dr. Thomas Passell of Materials and Chemistry Division of Electric Power Research Institute, Palo Alto, CA 94303 (18 September 1992).
[79] C. Bartolomeo, M. Fleischmann, G. Larramona, S. Pons, J. Roulette, H. Sugiura, and G. Preparata, Alfred Coehn and after: the alpha, beta, gamma of the palladium–ydrogen system, *Fourth Int. Conf. on Cold Fusion (ICCF-4)*, Lahaina, Maui, HI, USA, 1993, pp.19-1 to 19-47.
[80] F. Celani, A. Spallone, P. Tripodi, A. Petrocchi, D. di Gioacchino, P. Marini, V. di Stefano, S. Pace and A. Mancini, High power μs-pulsed electrolysis using palladium wires: evidence for a possible "phase" transition under deuterium overloaded conditions and related excess heat, *Fifth Int. Conf. on Cold Fusion (ICCF-5)*, Monte Carlo, Monaco, 9–13 April 1995, pp. 57–68.
[81] F. Celani, A. Spallone, P. Tripodi, A. Petrocchi, D. di Gioacchino, P. Marini, V. di Stefano, S. Pace and A. Mancini, Deuterium overloading of palladium wires by means of high power μs pulsed electrolysis and electromigration: suggestions of a phase transition and related excess heat, *Phys. Lett.* A **214** (1,2) (1996) 1–13.
[82] F. Celani, A. Spallone, P. Marini, V. di Stefano, M. Nakamura, A. Mancini, S. Pace, P. Tripodi, D. Di Gioacchino, C. Catena, G. D'Agostaro, R. Petraroli, P. Quercia, E. Righi and G. Trenta, High hydrogen loading into thin palladium wires through precipitate of alkaline–earth carbonate on the surface of cathode: evidence of new phases in the Pd--H system and unexpected problems due to bacteria contamination in the heavy water, *Eighth Int. Conf. on Cold Fusion (ICCF-8)*, Lerici (La Spezia), Italy, May 21--26, 2000, Conf. Proc., F. Scaramuzzi (Ed.), Vol. 70, pp. 181–190, 2001, Conference Proceedings of Compositori -- Società Italiana di Fisica, Bologna, Italy. ISBN 88-7794-256-8.
[83] F. Celani, O.M. Calamai, A. Spallone, A. Nuvoli, V. Andreassi, B. Ortenzi, F. Piastra, E. Righi, G. Trenta, E. Marano, P. Marini, V. di Stefano, M. Nakamura and E. Purchi, Development of a high temperature hybrid CMNS Reactor, *J. Condensed Matter Nucl. Sci.* **6** (2012) 24–33.
[84] E. Del Giudice, A. De Ninno, A. Frattolillo, G. Preparata, F. ScaramuzziA. Bulfone, M. Cola, C. Giannetti, The Fleischmann–Pons effect in a novel electrolytic configuration, *Proc. 8th Int. Conf. on Cold Fusion, ICCF-8*, Lerici, La Spezia, 21–26 May 2000, F. Scaramuzzi (Ed.), Conference Proceedings of Compositori -- Società Italiana di Fisica, Bologna, Italy. ISBN 88-7794-256-8, **70** (2001) 47–54.
[85] H. Wipf, *Electro- and Thermo-transport of Hydrogen in Metals*, G. Alefeld and J. Volkl (Eds.), Hydrogen in Metals II: Topics in Applied Physics, Vol. 29, Springer, Berlin, Heidelberg, New York, 1978, pp. 273–304.
[86] W.T. Read Jr., *Dislocations in Crystals*, McGraw-Hill New York, 1953
[87] W. Hayden, W.G. Moffatt and J. Wulff, *Structure and Properties of Materials,* Vol. III, *Mechanical Behavior,* Wiley, New York, 1965, pp. 63–64.
[88] R.E. Reed-Hill, *Physical Metallurgy Principles*, D. Van Nostrand, Princeton, NJ, 1964, pp. 139–143.
[89] M. Wen, L. Zhang, B. An, S. Fukuyama and K. Yokogawa**,** Hydrogen-enhanced dislocation activity and vacancy formation during nanoindentation of nickel, *Phys. Rev.* B **80** (2009) 094113.
[90] Note: The volume of the dislocation cell could also be considered as a cube of 1 μm on edge rather than a sphere, to be space filling, making its volume 1×10^{-18} m^3. Then the ratio of the volumes of 1 cm^3 to that of the dislocation cell is an even 1

$\times\ 10^{12}$(rather than 1.9×10^{12}) for estimating purposes.

[91]   B. D. Cullity, *Elements of X-ray Diffraction*, Addison-Wesley, Reading, MA, 1956 p. 117.

[92]   C. Sykes and H. Evans, The Transformations in the copper–gold alloy Cu_3Au, *J. Institute Metals* **58** (1936) 255.

[93]   Y. Fukai and N. Okuma, Formation of superabundant vacancies in Pd hydride under high hydrogen pressures, *Physl Rev Lett* **73** (12 (1994) 1640–1643.

[94]   Y. Fukai, Y. Shizuku and Y. Kurokawa, Superabundant vacancy formation in Ni–H alloys, *J. Alloys Compd.* **329** (2001) 195–201.

[95]   P.P. Fedorov and S. N. Volkov, Au–Cu phase diagram, *Russian J. Inorganic Chem.* **61**(6) (2016) 772–775. https://doi.org/10.1134/S0036023616060061.

[96]   H. Okamoto, D.J. Chakrabarti, D.E. Laughlin and T. Massalski, The Au−Cu (Gold–Copper) system, *J. Phase Equilibria (Bulletin of Alloy Phase Diagrams)* **8** (5) (1987) 454–474. DOI: 10.1007/BF02893155.

[97]   H. M. Syed, T.J. Gould, C.J. Webb and E. MacA. Gray, Superconductivityin palladium hydride and deuteride at 52– 61 K, Report for Queensland Micro- and Nanotechnology Centre, Griffith University, Nathan 4111, Brisbane, Australia. https://arxiv.org/ftp/arxiv/papers/1608/1608.01774.pdf , accessed 24 November 2018.

[98]   I. Anderson, The Dynamics of hydrogen in metals studied by inelastic neutron scattering, in Neutron *Scattering from Hydrogen in Metals*, A. Furrer (Ed.), World Scientific, Singapore, 1994, pp. 142–167.

[99]   K.P. Sinha, High temperature superconductivity in Pd–[H (D)]$_X$ system, *Natl. Academy Sci. Lett.* (India) **29** (3,4) (2006) 125–129: arXiv:cond-mat/0509596 [cond-mat.supr-con], https://arxiv.org/abs/cond-mat/0509596, accessed 25 November 2018.

[100] P.L. Hagelstein, Statistical mechanics model for the PdH and PdD phase diagram with both O-site and T-site occupation, *21st Int. Conf. Condensed Matter Nucl. Sci.* (ICCF-21), CO State University, Ft. Collins, CO, 3– 8 June 2018; *J. Condensed Matter Nucl. Sci.* (2019), in press.

[101] P.L. Hagelstein, Models for the phase diagram of palladium hydride including O-site and T-site occupation, *J. Condensed Matter Nucl. Sci.* **20** (2016) 54–80.

[102] P.L. Hagelstein, O-site and T-site occupation of α-phase PdH$_x$ and PdD$_x$, *J. Condensed Matter Nucl. Sci.* **17** (2015) 67–90.